

Single-cycle coherent terahertz-pulse propagation in rigid-rotor molecular mediaRobert Marskar^{1,2,*} and Ulf L. Österberg^{1,†}¹*Department of Electronics and Telecommunication, Norwegian University of Science and Technology, N-7491 Trondheim, Norway*²*SINTEF Energy Research, N-7034 Trondheim, Norway*

(Received 9 July 2015; published 24 August 2015)

We theoretically analyze linear and nonlinear coherent propagation of linearly polarized, plane-wave, resonant single-cycle terahertz pulses through spatially extended rigid-rotor molecular media. Our model incorporates mixed state medium preparation, nonperturbative nonlinearities, saturation, coherence, memory effects, and propagation, but ignores the effects of damping. Explicit solutions are reported in the linear propagation regime. These solutions are the multilevel superposition of linear, single-cycle 0π pulses, and appear as temporal beats in the time domain. For media initially in thermal equilibrium, the pulse and molecular beats are dispersive and broaden temporally with increased propagation distance. In the simplified limit of equal rotational line strength (an idealized situation), the emitted impulses are exact temporal copies of the input pulse. An efficient, scalable computational method for solving the reduced multilevel Maxwell-Bloch equations for molecular media is reported. This method is based on a standard differential method for the propagation equation together with an operator splitting method for the Bloch equations. It invokes neither the slowly varying envelope (SVEA) or rotating wave approximations (RWA), and incorporates a large number of possible energy eigenstates (we solve for 7744 levels). Case studies of nonlinear single-cycle pulse propagation are then provided by means of computer solutions. In the nonlinear regime, we observe strong molecular orientations and suppression of the pulse and orientational revivals predicted by linear theory. For sufficiently strong pulses, coherent bleaching effects lead to increased transmission of the driving pulse, which also bears signs of self-modulation and carrier-shock formation.

DOI: [10.1103/PhysRevA.92.023843](https://doi.org/10.1103/PhysRevA.92.023843)

PACS number(s): 42.25.Bs, 42.65.Re, 42.50.Md

I. INTRODUCTION

Pulsed terahertz (THz) technology [1] is emerging as an attractive research field with various applications in biomedical imaging [2], spectroscopy [3,4], and molecular orientation [5–16]. In contrast to material excitations using optical radiation, which predominantly excites valence electrons in the ~ 2 -eV range, electromagnetic THz waves excite low-energy modes such as molecular rotations [7], lattice vibrations [17], and spin waves [18]. It is, for example, the rotational transitions in light molecules that make THz a candidate for nonionizing medical imaging of soft tissue, while several other key applications, such as quantum information [19], chemical selectivity [20], population control [21], etc., rely on an anisotropic molecular angular distribution. Other researchers aim at using angularly localized molecules as an intermediate preparation step for initiating strong field ionization [22] or high harmonic generation (HHG) [23]. Although the field of THz-induced molecular orientation has grown rapidly over the past decade, the first observation of THz-induced orientation of polar molecules appears in the early experiments by Harde *et al.* [24] and Harde and Grischkowsky [25]. Classically, macroscopic molecular orientations are initiated by the torque a polarized external field exerts through the permanent dipole moment of the molecule. For linearly polarized, time-varying fields, the torsional force is directed in the polar plane of the molecules and acts to orient them along the instantaneous field direction. After the pulse has passed, the free induction decay (FID) polarization signal of the molecules deteriorates

rapidly due to destructive interference between an infinite number of excited rotational modes, analogous to the FID of an excited inhomogeneously broadened two-level quantum system. Quantum mechanically, a resonant pulse coherently excites a finite number of possible angular momentum modes. In the absence of an external field, the interference among the variously excited transitions also leads to initial suppression of the free-induction signal. However, due to the discreteness of the quantum-mechanical rigid rotor, the molecules reorient at certain rephasing periods and radiate in phase at equally spaced time bursts. The space-time behavior of the bursts describes the fidelity of the molecular orientation, and is of practical interest in both the linear and nonlinear excitation regimes.

Propagation of resonant THz pulses through an extended molecular medium has, to the best of our knowledge, not been considered to date. Electromagnetic THz waves overlap with the rotational transitions of light, polar molecules. Examples of such molecules are the hydrogen halides [e.g., hydrogen fluoride (H=F) and carbonyl sulfide (O=C=S)]. In the vapor phase, the relaxation times of these transitions are comparatively long with respect to the THz pulse duration ($\lesssim 1$ ps). A THz pulse can therefore excite large-amplitude, long-lived coherent molecular transients. A theoretical description must correspondingly incorporate memory effects, saturation and quantum coherence, rather than employing models based on parametric wave amplification, or on pulse intensities and rate equations. It is clear that although the backaction of the molecular response on the propagating field is of obvious importance to the above mentioned applications, and provide more than enough justification for a theoretical study, a first-principles approach is interesting also in its own right.

In this paper, we investigate the propagation of linearly polarized single-cycle THz pulses moving through an extended

*robert.marskar@iet.ntnu.no, robert.marskar@sintef.no

†ulf.osterberg@iet.ntnu.no

rigid-rotor molecular medium. Our approach is semiclassical; the THz field is imposed as a spatially and temporally varying classical (i.e., nonquantized) field, and the molecules are described using quantum theory. This model differs from theoretical models employed in laser alignment studies with regard to incorporation of the radiation reaction feature of the molecules, and its effect on the propagated field. Traditional semiclassical pulse propagation models based on the simplifying slowly varying envelope and rotating wave approximations are stretched to their limits—or even broken—in the single-cycle regime that we study. Moreover, the octave-wide spectra of such pulses break with the bandwidth constraints that are necessary in the conventional approximation of the Schrödinger equation to a few-level Bloch system. For rigid-rotor molecules, the theoretical complexity is additionally reinforced by the level degeneracy of higher angular momentum states. It has been shown that nonresonant pulse interaction with such molecules may be treated in a simplified model using a delayed Raman response, but the calculation technique is limited to times much shorter than the rotational revival period and only capture the leading edge of the pulse [26]. In addition, the expressions for the optical response are then entirely classical, leaving out effects like molecular coherence, saturation, and quantum discreteness. An analysis beyond these limitations is technically demanding, but feasible. In the face of these challenges we resort to numerical computations and extend the theoretical framework of coherent pulse propagation in several directions. Firstly, we establish a unidirectional multilevel theoretical model for the propagation of linearly polarized single-cycle pulses through rigid-rotor media. We derive exact solutions in the linear, sharp-line limit. An interesting solution is encountered when the line intensities of each transition are equal (a theoretical situation), in which case the rotational wave packets emit exact temporal copies of the input pulse. Secondly, starting from a propagation equation valid for single-cycle pulse durations, we formulate a scalable numerical algorithm for spatiotemporal integration of the nonlinear equations of motion. Such calculations are usually performed in the framework of the finite-difference time-domain (FDTD) method reported by Ziolkowski *et al.* [27], which is based on the full Maxwell equations coupled with quantum theory under the two-level restriction. Ziolkowski's original method has been adopted by others [28–30] and has also been extended to homogeneously and inhomogeneously damped multilevel media [31–34]. However, direct Maxwell methods are numerically limited to short propagation lengths, enforced by the requirement of a spatial step size, which must be smaller than a wavelength. It is well known, however, that Maxwell's wave equation may be reduced to a unidirectional propagation equation outside the conventional slowly varying envelope approximation (see, e.g., [35–39]), but coupling of these equations to resonant response models has not been considered to date. In contrast, the novelty of our method, which pertains to the electric field rather than the concept of a pulse envelope, lies in its applicability to single-cycle pulse propagation over long distances for many-level media. Here, we numerically integrate over $J = 87$ degenerate rotational levels, corresponding to $(J + 1)^4 \approx 60 \times 10^6$ individual density matrix elements. In addition, the numerical methods reported are immediately

extendible to any type of finite-dimensional Bloch system, and thus offer a pathway for investigating other types of molecular excitations. Thirdly, we report on computer solutions for field and molecules in the nonlinear propagation regime. We observe that as the amplitude of the input THz pulse increases, the molecules are strongly orientated and the pulse revivals predicted by linear theory are considerably suppressed. For sufficiently strong pulses, coherent bleaching leads to increased transmission of the driving pulse, which also shows signatures of self-modulation and carrier-shock formation.

This paper is organized as follows. In Sec. II, we present our theoretical model and basic definitions. This model is linearized and further analyzed in Sec. III where we report on exact solutions. In Sec. IV, we present a computational method for spatiotemporal integration of the parametrically coupled equations of motion, before presenting computer solutions for nonlinear propagation in Sec. V. Our results are summarized in Sec. VI, and we mention a few possible future extensions of this work.

II. PHYSICAL MODEL

A. Maxwell's equations

In the laboratory frame, we presume that the THz pulse is linearly polarized along z and propagates along $+x$ without significant coupling in the transverse plane. The propagation of the electric field $\mathbf{E} = E(t, x)\hat{z}$ is described by the scalar wave equation

$$\left(\frac{\partial^2}{\partial t^2} - c^2 \frac{\partial^2}{\partial x^2}\right)E(t, x) = \frac{1}{\epsilon_0} \frac{\partial^2 P(t, x)}{\partial t^2}, \quad (1)$$

where $\mathbf{P} = P(t, x)\hat{z}$ is the molecular polarization. Equation (1) is a bidirectional wave equation supporting propagation along $\pm x$ and is susceptible to numerical integration, but requires spatial sampling finer than a wavelength. To reduce the numerical cost inherent in Eq. (1), it is necessary to neglect the possibility of backward wave propagation along $-x$. Excitations of backward traveling waves are interesting in their own right, and may have profound effects [40–42], but only their absence is desired here. The following scaling argument due to Bullough *et al.* [43] applies. Scale E and P by constants E_c and P_c such that

$$\mathcal{E} = \frac{E}{E_c}, \quad (2a)$$

$$\mathcal{P} = \frac{P}{P_c} \quad (2b)$$

are quantities of order unity. Introduce the new coordinates $\tau_{\pm} = t \pm x/c$, $c\partial/\partial x = \partial/\partial\tau_+ - \partial/\partial\tau_-$, $\partial/\partial t = \partial/\partial\tau_+ + \partial/\partial\tau_-$, which yields for Eq. (1)

$$2\frac{\partial^2}{\partial\tau_-\partial\tau_+}\mathcal{E} = -\frac{\varepsilon}{2}\left(\frac{\partial}{\partial\tau_-} + \frac{\partial}{\partial\tau_+}\right)^2\mathcal{P}, \quad (3)$$

where $\varepsilon = P_c/(\epsilon_0 E_c)$ is presumed to be a small quantity. Look for solutions with dominant forward traveling parts with

forward and backward traveling perturbations:

$$\mathcal{E} = \mathcal{E}_0(\tau_-) + \varepsilon \mathcal{E}_1(\tau_-, \tau_+) + \varepsilon^2 \mathcal{E}_2(\tau_-, \tau_+) + \dots, \quad (4a)$$

$$\mathcal{P} = \mathcal{P}_0(\tau_-) + \varepsilon \mathcal{P}_1(\tau_-, \tau_+) + \varepsilon^2 \mathcal{P}_2(\tau_-, \tau_+) + \dots. \quad (4b)$$

To first order in ε , Eq. (3) yields

$$2\varepsilon \frac{\partial \mathcal{E}_1}{\partial \tau_+} = -\frac{\varepsilon}{2} \frac{\partial \mathcal{P}_0}{\partial \tau_-} + O(\varepsilon^2), \quad (5)$$

which is equivalent to

$$2 \frac{\partial}{\partial \tau_+} (\mathcal{E}_0 + \varepsilon \mathcal{E}_1) = -\frac{\varepsilon}{2} \left(\frac{\partial}{\partial \tau_+} + \frac{\partial}{\partial \tau_-} \right) \mathcal{P}_0 + O(\varepsilon^2). \quad (6)$$

Reverting back to the original coordinates and fields, we find

$$\left(\frac{\partial}{\partial t} + c \frac{\partial}{\partial x} \right) E = -\frac{1}{2\varepsilon_0} \frac{\partial P}{\partial t}. \quad (7)$$

We switch to a traveling reference frame by introducing the retarded time $\tau = t - x/c$, which transforms Eq. (7) into

$$\frac{\partial E(\tau, x)}{\partial x} = -\frac{1}{2\varepsilon_0 c} \frac{\partial P(\tau, x)}{\partial \tau}. \quad (8)$$

Physically, Eq. (8) is valid only when the polarization is small compared to the electric field, or equivalently when changes to E induced by the material are negligible over a wavelength [35]. These conditions hold for a wide class of experiments. Strictly speaking, Eqs. (1) and (8) are not valid for subcycle pulses because diffraction-induced transformations then occur due to the different Rayleigh lengths of each frequency component contained in the pulse, which will chirp the pulse even for propagation in free space [44]. Analogous to the results obtained by invoking slowly varying envelope approximation, Eq. (8) describes the spatiotemporal evolution in terms of the delayed time τ , an equation which is computationally more tractable than Eq. (1). The price to pay for this simplification is the neglect of interaction with self-induced backward traveling waves [40–42].

B. Optical Bloch equations

We assume that the material is described by a collection of noninteracting molecules, and that the Born-Oppenheimer approximation is valid. This decouples the electronic, vibrational, and rotational degrees of freedom. In the absence of interactions that excite ro-vibrational or vibronic motions, the molecule remains in its initial electronic and vibrational state, and only the rotational part of the molecule is affected by the externally applied THz field. For greatest simplicity, we disregard centrifugal distortion and model this part of the molecule as a rigid rotor (see Fig. 1).

The interaction between the rotor molecules and the external field E is described by the Hamiltonian

$$\begin{aligned} H &= \frac{\mathbf{J}^2}{2I} - \boldsymbol{\mu} \cdot \mathbf{E} \\ &= \sum_{jm} \hbar \omega_j |jm\rangle \langle jm| - E \sum_{\substack{jm \\ j'm'}} \mu_{jm, j'm'}^{(z)} |jm\rangle \langle j'm'|, \end{aligned} \quad (9)$$

where \mathbf{J} is the angular momentum operator and I is the moment of inertia of the molecule. The first term on the right-

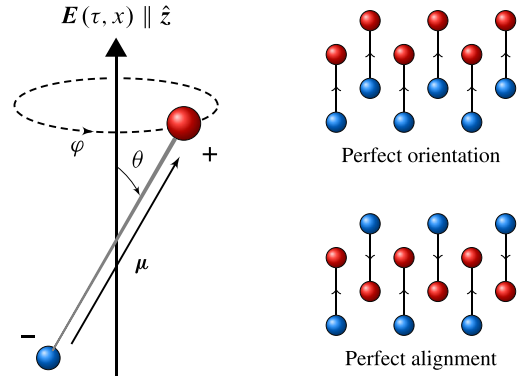


FIG. 1. (Color online) Rigid-rotor molecular model. The angles θ and φ define the polar and azimuthal angles the molecular axis, defined as the vector from the negative to the positive charge, with respect to the field polarization. The polarization of the E field is space-fixed along \mathbf{z} for all times.

hand side of Eq. (9) represents the free rotational Hamiltonian H_0 of the molecule; the second represents the interaction with the external field. In the second line of Eq. (9), the Hamiltonian is expanded in the spherical harmonic eigenstates $|jm\rangle$ that are simultaneous eigenfunctions of \mathbf{J}^2 and J_z with eigenvalues

$$\mathbf{J}^2 |jm\rangle = \hbar^2 j(j+1) |jm\rangle, \quad (10a)$$

$$J_z |jm\rangle = \hbar m |jm\rangle, \quad (10b)$$

where $\hbar m$ is the projection of the angular momentum of a rotational eigenstate $|jm\rangle$ onto the space-fixed z axis. The dipole moment operator is expanded in the same basis with $\mu^{(z)}$ as the projection of $\boldsymbol{\mu}$ onto $\hat{\mathbf{z}}$. Magnetic field couplings are neglected and the rotor eigenfrequencies are therefore independent of the quantum number m , and equal to

$$\omega_j = \frac{1}{\hbar} \langle jm | \frac{\mathbf{J}^2}{2I} | jm \rangle = \frac{j(j+1)}{2} \Delta\omega, \quad (11)$$

where $\Delta\omega = \hbar/(2I)$ is the fundamental quantum beat frequency of the molecule. In the rigid-rotor approximation, the energy spacing between adjacent rotational levels is $\hbar(\omega_{j+1} - \omega_j) = (j+1)\hbar\Delta\omega$, and the linear rotational spectrum consists of many equally spaced spectral absorption lines, as shown in Fig. 2.

The rotational part of the density operator is defined as the ensemble average

$$\rho(\tau, x) = \sum_k p_k |\Psi_k\rangle \langle \Psi_k|, \quad (12)$$

where $\sum_k p_k = 1$ is a probability normalization requirement and the pure state $|\Psi_k\rangle$ is a superposition of jm modes. The sum runs over possible microstates in the ensemble. The time evolution of the molecules is described by the von Neumann equation

$$i\hbar \frac{d\rho}{d\tau} = [H_0, \rho] - E[\mu^{(z)}, \rho]. \quad (13)$$

This paper investigates the coherent regime where the pulse duration is considerably shorter than any relaxation rates. Damping terms are therefore omitted in Eq. (13). It is

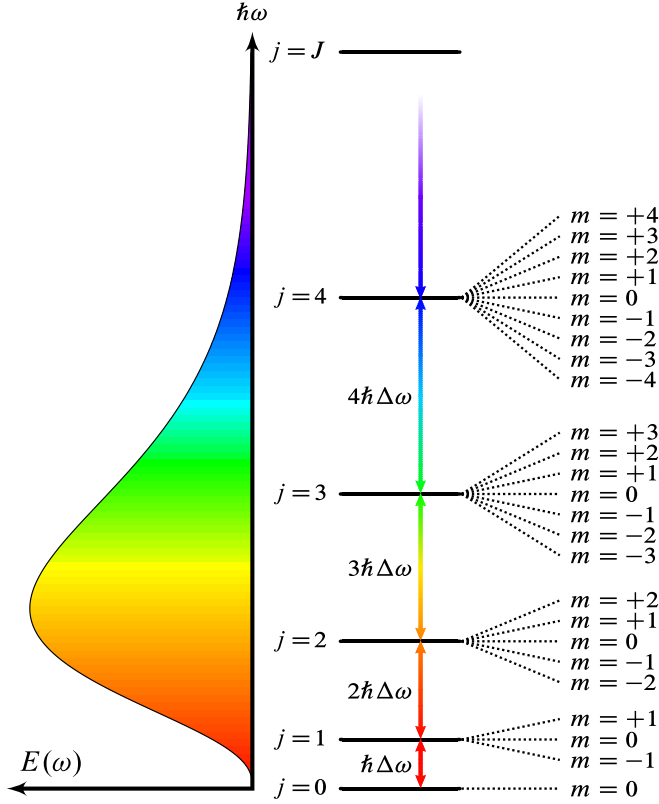


FIG. 2. (Color online) Single-cycle pulse interaction with a rigid-rotor molecule where adjacent energy states are connected via electric dipole transitions. The pulse spectrum is broad enough to simultaneously excite a large number of molecular eigenstates. Each energy level j contains $2j + 1$ degenerate rotor states.

nonetheless necessary to employ a density matrix formalism since the molecules are prepared without initial coherence. To solve Eq. (13), we expand the density operator ρ in the orthonormal eigenset $\{|jm\rangle\}$ and solve for the expansion coefficients, reducing Eq. (13) to a time-dependent finite-dimensional matrix problem. Following convention [43,45,46], Eqs. (8) and (13) are termed the reduced Maxwell-Bloch (RMB) equations.

From these basic definitions, the essential physical mechanism for field-free wave-packet revival can be understood straightforwardly. Assume that the molecules are linearly or nonlinearly excited by a pulse $E(\tau)$, which is turned off at time $\tau = 0$. Since $H = H_0$ is constant for $\tau > 0$, the exact solution to Eq. (13) for all times $\tau > 0$ is

$$\rho(\tau) = \exp\left(-i\frac{H_0\tau}{\hbar}\right)\rho(0)\exp\left(i\frac{H_0\tau}{\hbar}\right), \quad (14)$$

or in index form

$$\rho_{jm,j'm'}(\tau) = \exp\left(\frac{i\Delta\omega[j'(j'+1) - j(j+1)]}{2}\tau\right)\rho_{jm,j'm'}(0). \quad (15)$$

Since j, j' are integers, then $j(j+1) - j'(j'+1)$ is always an even number, and the argument of the exponential function is therefore always an integer multiple of $i\Delta\omega\tau$. For longer times, $\tau \rightarrow \tau + kT_b$, one then finds $\rho(\tau + kT_b) = \rho(\tau)$ since

$\exp[2\pi i k] = 1$. Consequently, wave-packet rephasing always occurs when the eigenvalues of H_0 are harmonic multiples of a common frequency.

The solution for $\rho(\tau, x)$ completely describes the rotational state of the medium and the solution for $E(\tau, x)$ the propagation of the external field. Apart from the linear interaction regime, solutions for both variables must be obtained with numerical calculations. Unlike simple two- or three-level media, ρ has a large number of possible nonzero entries, and the spatiotemporal evolution must therefore be described in terms of experimental observables rather than referring to ρ directly.

1. Polarization

The nonzero entries of the dipole moment operator are [47]

$$\mu_{jm,j+1m}^{(z)} = \mu_p \sqrt{\frac{(1+j)^2 - m^2}{(2j+3)(2j+1)}}, \quad (16)$$

where μ_p is the permanent dipole moment of the molecule. For linearly polarized light fields, the optical selection rules $j \rightarrow j \pm 1, m \rightarrow m$ apply.

The quantum numbers j, m are convenient quantum numbers since the molecular motion is confined to j space, while no coherence is established between states with different m numbers. In the suitable coordinate system where E is polarized along z for all times, the interaction potential $\mu \cdot E$ is independent of φ . The torque $N = \mu \times E$ exerted by the field on the molecule locks the THz-induced rotations in the polar plane,

$$N = -\mu_p E(t) \sin\theta \hat{\varphi}. \quad (17)$$

System rotations of the molecule around the polarization axis are invariant leaving the molecules free to rotate in the azimuthal plane. It may be verified that $d_\tau \langle J_z \rangle = 0$ for Eq. (13) and if $\langle J_z \rangle$ is initially zero, the azimuthal rotations average out, and the macroscopic polarization is then always $P = P\hat{z}$.

In all of the following, we denote $\mu^{(z)} \rightarrow \mu$ to condense notation. The molecular coupling to the external field occurs via the polarization $P = \mathcal{N} \langle \mu \rangle = \mathcal{N} \text{Tr}(\rho\mu)$, where \mathcal{N} is the number density of the medium. Using $\mu = \mu_p \cos\theta$ yields

$$P = \mathcal{N} \mu_p \langle \cos\theta \rangle. \quad (18)$$

Equivalently, using the transition rules above,

$$P = \mathcal{N} \sum_{j=0}^{J-1} \sum_{m=-j}^j \mu_{jm,j+1m} \rho_{j+1m,jm} + \mu_{j+1m,jm} \rho_{jm,j+1m} \quad (19)$$

in index form.

2. Energy conservation

During propagation, energy is transferred between field and medium. By using $\frac{\partial}{\partial \tau} \mathcal{N} \langle H \rangle = -(\frac{\partial}{\partial \tau} E)P$, Eqs. (8) and (13) may be combined to a common energy conservation equation:

$$\epsilon_0 c \frac{\partial}{\partial x} E^2(\tau, x) + \mathcal{N} \frac{\partial \langle H_0 \rangle(\tau, x)}{\partial \tau} = 0, \quad (20)$$

where $\epsilon_0 c E^2$ is the instantaneous intensity of the external field and $\mathcal{N} \langle H_0 \rangle$ is the internal molecular energy. In the undamped

limit considered here, optical transparency is mathematically inevitable since excited rotor molecules radiate indefinitely due to the absence of damping terms. This manifests itself as an infinitely long coherent transient in pulse and medium, while in reality damping always takes place for sufficiently long times, and the pulse duration remains finite. Our solutions are only valid for time scales considerably shorter than any relaxation times. The concept of “total energy transmission” is not applicable to our computer simulations because the pulse tail is, out of computational necessity, truncated at a finite integration time. Equation (20) may nevertheless be applied unambiguously provided that relaxation times remain comparatively long.

3. Position space

It is convenient to represent the molecular state in the infinite-dimensional coordinate space. The projection of the eigenstates $|jm\rangle$ into position space \mathbf{r} is

$$\langle \hat{\mathbf{n}} | jm \rangle = Y_j^m(\theta, \varphi), \quad (21)$$

where $\hat{\mathbf{n}}$ is a unit vector along (θ, φ) , $Y_j^m(\theta, \varphi)$ is the complex spherical harmonic

$$Y_j^m(\theta, \varphi) = (-1)^m \sqrt{\frac{(2j+1)(j-m)!}{4\pi(j+m)!}} P_j^m(\cos\theta) e^{im\varphi}, \quad (22)$$

and $P_j^m(\cos\theta)$ is an associated Legendre polynomial. The probability density ϱ is defined

$$\varrho(\tau, x; \theta, \varphi) = \langle \hat{\mathbf{n}} | \rho(\tau, x) | \hat{\mathbf{n}} \rangle = \sum_k P_k |\Psi_k(\tau, x; \hat{\mathbf{n}})|^2, \quad (23)$$

where $\Psi_k(\tau, x; \hat{\mathbf{n}}) = \langle \hat{\mathbf{n}} | \Psi_k(\tau, x) \rangle$. Expanding Ψ_k into spherical harmonics yields

$$\varrho(\tau, x; \theta, \varphi) = \sum_{\substack{jm \\ j'm'}} \rho_{jm, j'm'} Y_j^m Y_{j'}^{m'*}. \quad (24)$$

The notation $(\tau, x; \theta, \varphi)$ specifies that τ and x are external laboratory coordinates, and (θ, φ) are internal coordinates for the molecules. Thus $\varrho(\tau, x; \theta, \varphi)$ describes the probability of observing the molecules along (θ, φ) a propagation distance x into the medium at time τ (see Fig. 1). Since $\mu_{jm, j'm'} = 0$ for $m \neq m'$, we also have $\rho_{jm, j'm'} = 0$ for $m \neq m'$ when the medium starts out in a completely mixed state, which we will presume throughout this article. The φ dependence (but not m dependence) can be removed from Eq. (24) and ϱ changes to

$$\varrho(\tau, x; \theta) = \sum_{j, j', m} \rho_{jm, j'm} Y_j^m Y_{j'}^{m*}. \quad (25)$$

For numerical convenience, Eq. (25) is compactly written

$$\varrho(\tau, x; \theta) = \rho(\tau, x) : G(\theta), \quad (26)$$

where $:$ is the Frobenius product, and G is a matrix operator with entries

$$G_{jm, j'm}(\theta) = Y_j^m(\theta, \varphi) Y_{j'}^{m*}(\theta, \varphi). \quad (27)$$

For density operators, ϱ is analogous to the probability density $|\Psi(\hat{\mathbf{n}})|^2 = |\langle \hat{\mathbf{n}} | \Psi \rangle|^2$ for a pure state $|\Psi\rangle$. Conservation of

probability implies that

$$\int_0^\pi \varrho(\tau, x; \theta) \sin\theta d\theta = \frac{1}{2\pi}. \quad (28)$$

A realistic theoretical prediction for the molecular shape must incorporate Zeeman levels even when no transitions between the various harmonic ladder systems associated with different quantum numbers m occur. For example, for media in thermal equilibrium, Unsöld's theorem shows that $\varrho \rightarrow 1/(4\pi)$ only when the Zeeman levels are equally populated for each j (spherical symmetry of ϱ indicates that the molecular axes are distributed isotropically over the unit sphere).

4. Molecular alignment

Transient optical birefringence is measurable [48] and proportional to the quantity

$$\langle \cos^2\theta \rangle = \sum_{jm} \rho_{jm, jm} V_{jm, jm} + \rho_{jm, j\pm 2m} V_{j\pm 2m, jm}, \quad (29)$$

where

$$V_{jm, jm} = \frac{1}{3} \left[1 + 2 \frac{j(j+1) - 3m^2}{(2j+3)(2j-1)} \right], \quad (30a)$$

$$V_{j-2m, jm} = \sqrt{\frac{(j-1)^2 - m^2}{(2j-1)^2} \frac{j^2 - m^2}{(2j-3)(2j+1)}}. \quad (30b)$$

The observable $\langle \cos^2\theta \rangle$ may be partitioned into population and coherences as $\langle \cos^2\theta \rangle_p = \sum_{jm} \rho_{jm, jm} V_{jm, jm}$ and $\langle \cos^2\theta \rangle_c = \sum_{jm, j'=j\pm 2} \rho_{jm, j'm} V_{j'm, jm}$ [49]. For a medium with isotropically distributed magnetic sublevels for each j , $\langle \cos^2\theta \rangle_p$ evaluates to $1/3$.

Equivalently, the orientation and alignment are described in terms of the Legendre moments

$$\langle P_\kappa(\cos\theta) \rangle = \sum_{j, j', m} \rho_{jm, j'm} \langle j'm | P_\kappa(\cos\theta) | jm \rangle = \rho : L, \quad (31)$$

where, of course, $\langle P_\kappa(\cos\theta) \rangle$ is additionally dependent on the extensive variables (τ, x) via ρ . Using the Wigner $3j$ symbols, the coefficients of the matrix L are analytically expressible,

$$L_{jm, j'm} = (-1)^m \sqrt{(2j'+1)(2j+1)} \times \begin{pmatrix} j' & k & j \\ 0 & 0 & 0 \end{pmatrix} \begin{pmatrix} j' & k & j \\ -m & 0 & m \end{pmatrix}. \quad (32)$$

The odd-even properties of $P_\kappa(\cos\theta)$ imply that odd Legendre moments measure the orientation and even moments measure the alignment. Special values are $\langle P_0 \rangle = 1$, $\langle P_1 \rangle = \langle \cos\theta \rangle$, and $\langle P_2 \rangle = (3\langle \cos^2\theta \rangle - 1)/2$. By the selection rules of the Wigner $3j$ symbols, odd moments of $\langle P_\kappa(\cos\theta) \rangle$ contain only coherences up to order $|j' - j| \leq \kappa$. In addition, even moments contain populations up to the same order.

III. LINEAR SOLUTIONS

A. Linearization

Analytic solutions to Eq. (8) exist in the linear regime when ρ is expanded to first order using standard

quantum-mechanical time-dependent perturbation theory [48]. We denote the order of the perturbation expansion by incorporating a bracketed superscript on ρ (e.g., $\rho^{[0]}$). The relevant differential equations are the time evolution equations for the population elements:

$$\begin{aligned} \partial_\tau \rho_{jm,jm} &= i \frac{E}{\hbar} \mu_{jm,j+1m} \rho_{j+1m,jm} \\ &+ i \frac{E}{\hbar} \mu_{jm,j-1m} \rho_{j-1m,jm} + \text{c.c.}, \end{aligned} \quad (33)$$

where c.c. indicates the complex conjugate, and the polarization coherence elements

$$\begin{aligned} \partial_\tau \rho_{j+1m,jm} &= -i(\omega_{j+1} - \omega_j) \rho_{j+1m,jm} \\ &+ i \frac{\mu_{j+1m,jm} E}{\hbar} (\rho_{jm,jm} - \rho_{j+1m,j+1m}) \\ &+ i \frac{E}{\hbar} \mu_{j+1m,j+2m} \rho_{j+2m,jm} \\ &- i \frac{E}{\hbar} \mu_{j-1m,jm} \rho_{j+1m,j-1m}. \end{aligned} \quad (34)$$

The terms on the right-hand side of Eq. (34) containing the two-photon coherences $\rho_{j+2m,jm}$, $\rho_{j+1m,j-1m}$ indicate the presence of a rotational Raman coupling, which we disregard in the linear approximation. Assuming that the populations are not altered by the pulse, the first-order perturbative solution for the polarization coherence $\rho_{j+1m,jm}$ is

$$\begin{aligned} \rho_{j+1m,jm}^{[1]} &= i \frac{\mu_{j+1m,jm} (\rho_{jm,jm}^{[0]} - \rho_{j+1m,j+1m}^{[0]})}{\hbar} \\ &\times \int_{-\infty}^{\tau} E(\tau') e^{i(\omega_{j+1} - \omega_j)(\tau' - \tau)} d\tau', \end{aligned} \quad (35)$$

where $\rho^{[0]} = \rho(\tau = -\infty, x)$ is the completely mixed initial state $\rho_{jm,j'm'}^{[0]} = 0$ for all $jm \neq j'm'$. We may evaluate the validity of Eq. (35) in the following way. Inserting Eq. (35) into the right-hand side of Eq. (33) followed by integration with respect to time gives the first-order solution

$$\begin{aligned} \rho_{jm,jm}^{[1]} &= \rho_{jm,jm}^{[0]} - \frac{|\mu_{jm,j+1m}|^2 (\rho_{jm,jm}^{[0]} - \rho_{j+1m,j+1m}^{[0]})}{\hbar^2} \\ &\times \int_{-\infty}^{\tau} d\tau' \int_{-\infty}^{\tau'} d\tau'' E(\tau') E(\tau'') e^{i(\omega_{j+1} - \omega_j)(\tau' - \tau'')} \\ &+ \dots \end{aligned} \quad (36)$$

The dots indicate the presence of additional terms that are of the same order. The largest possible contribution from the integrals is estimated by the triangle inequality $|\int_{-\infty}^{\tau} E(\tau') \exp[i(\omega_{j+1} - \omega_j)\tau'] d\tau'| \leq \int_{-\infty}^{\tau} d\tau' |E(\tau')|$. A boxcar pulse $|E(\tau)| = E_0$ for $0 \leq \tau \leq T$ may be used to approximate the magnitude of a single-cycle pulse with duration T . Substitution into the above integral expression yields, for $\tau \geq T/2$,

$$\begin{aligned} \rho_{jm,jm}^{[1]} - \rho_{jm,jm}^{[0]} &\leq (\rho_{jm,jm}^{[0]} - \rho_{j+1m,j+1m}^{[0]}) \\ &\times \frac{|\mu_{jm,j+1m}|^2 E_0^2 T^2}{2\hbar^2} + \dots \end{aligned} \quad (37)$$

The linear approximation is valid if the right-hand side of Eq. (37) is negligibly small with respect to $\rho_{jm,jm}^{[0]}$, which

essentially is a small area [50] approximation. Equation (37) then shows that the linear approximation is applicable if

$$\frac{\rho_{jm,jm}^{[0]} - \rho_{j+1m,j+1m}^{[0]} |\mu_{jm,j+1m}|^2 E_0^2 T^2}{\rho_{jm,jm}^{[0]} 2\hbar^2} \ll 1, \quad (38)$$

in which case Eq. (35) may be used to calculate the polarization coherences and the spatiotemporal evolution of the pulse. Note that the quantity $\mu_{jm,j+1m} E_0 T / \hbar$ is essentially the conventional pulse area associated with a $j \rightarrow j+1$ transition for linearly polarized fields; the presence of the population terms indicates that the initial population is distributed into several molecular orbitals. This leads to a natural definition of a normalized pulse area for the $j \rightarrow j+1$ transition:

$$\Theta_j^m \equiv \frac{\rho_{jm,jm}^{[0]} - \rho_{j+1m,j+1m}^{[0]} |\mu_{jm,j+1m}|^2 E_0^2 T^2}{\rho_{jm,jm}^{[0]} 2\hbar^2}, \quad (39)$$

in which case the linear approximation is valid if $\Theta_j^m \ll 1$ for all jm .

To help clarify some of the approximations invoked in deriving analytical solutions, we also consider in the next two subsections the effects of homogeneous damping by introducing phenomenological terms $-\gamma \rho_{j+1m,jm}$ into the right-hand side of Eq. (34), where γ is the decoherence rate. In the frequency domain, Eq. (35) becomes

$$\rho_{j+1m,jm}^{[1]}(\omega) = \frac{\mu_{j+1m,jm} (\rho_{jm,jm}^{[0]} - \rho_{j+1m,j+1m}^{[0]})}{\hbar(\omega - (\omega_{j+1} - \omega_j) - i\gamma)} E(\omega, x), \quad (40)$$

which describes a quantum-mechanical Lorentz resonance.

B. Exact linear solution: relation to the 0π pulse

The linearized equations of motion are solved by transforming Eq. (8) to the frequency domain,

$$\partial_x E(\omega) = -\frac{i\omega}{2\epsilon_0 c} P(\omega). \quad (41)$$

The expression for the polarization is obtained by inserting Eq. (40) into Eq. (19), and inserting the resulting expression for $P(\omega)$ into Eq. (41) yields an evolution equation for E in the frequency domain, with the exact solution

$$E(\omega, x) = \exp\left(\sum_{j=0}^{J-1} \frac{-\omega \beta_j x}{\omega_{j+1} - \omega_j} [A_j^-(\omega) - A_j^+(\omega)]\right) E(\omega, 0), \quad (42)$$

where

$$A_j^\pm(\omega) = \frac{1}{i\omega \pm i(\omega_{j+1} - \omega_j) + \gamma}. \quad (43)$$

Equation (42) shows that E obeys a frequency domain Beer's law where each frequency component decays exponentially with distance. Using Eqs. (11) and (16), we have summed over the Zeeman levels. When these are populated isotropically for each j , the coefficients β_j are

$$\beta_j = \frac{\mathcal{N} \mu_p^2 (j+1)^2 \Delta\omega (\rho_{j,j}^{[0]} - \rho_{j+1,j+1}^{[0]})}{6\epsilon_0 \hbar c}, \quad (44)$$

where $\rho_{j,j}^{[0]}$ is the initial population of level j for any m . To return to the time domain, the exponential is expanded in its Taylor series and cross terms $A_j^\pm A_j^\mp$ are neglected since $A^\pm(\omega)$ is sharply peaked around $\mp(\omega_{j+1} - \omega_j)$ in the sharp-line limit $\gamma \ll \omega_{j+1} - \omega_j$. By the same argument,

$$\frac{\omega}{i\omega \pm i(\omega_{j+1} - \omega_j) + \gamma} \approx \frac{\mp(\omega_{j+1} - \omega_j)}{i\omega \pm i(\omega_{j+1} - \omega_j) + \gamma}. \quad (45)$$

Transforming back to the time-domain yields

$$E(\tau, x) = E(\tau, 0) + \sum_{j=0}^{J-1} \int_{-\infty}^{\infty} \sum_{n=1}^{\infty} \frac{(-\beta_j x)^n}{n!} [A_{jn}^+(\tau') + A_{jn}^-(\tau')] \times E(\tau - \tau', 0) d\tau', \quad (46)$$

where $A_{jn}^\pm(\omega) \equiv [A_j^\pm(\omega)]^n$. In the time domain,

$$A_{jn}^\pm(\tau) = \frac{\tau^{n-1}}{(n-1)!} e^{-\gamma\tau \mp i(\omega_{j+1} - \omega_j)\tau} u(\tau), \quad (47)$$

where $u(\tau)$ is the unit step function. The first term $E(\tau, 0)$ in Eq. (46) represents free translation of the pulse in the absence of a medium and the convolution integral represents the reshaping of the pulse due to the molecular response. Inserting Eq. (47) into Eq. (46) yields

$$E(\tau, x) = E(\tau, 0) + 2 \sum_{j=0}^{J-1} \int_0^{\infty} \sum_{n=1}^{\infty} \frac{(-\beta_j \tau' x)^n}{n!(n-1)!} \frac{1}{\tau'} \times e^{-\gamma\tau'} \cos[(\omega_{j+1} - \omega_j)\tau'] E(\tau - \tau', 0) d\tau'. \quad (48)$$

The sum over n evaluates to [51]

$$\sum_{n=1}^{\infty} \frac{(-\beta_j \tau' x)^n}{n!(n-1)!} \frac{1}{\tau'} = -\sqrt{\frac{\beta_j x}{\tau'}} J_1(2\sqrt{\beta_j \tau' x}), \quad (49)$$

where $J_1(x)$ is a Bessel function of the first kind. The final solution for $E(\tau, x)$ in the linear limit is

$$E(\tau, x) = E(\tau, 0) - 2 \sum_{j=0}^{J-1} \int_0^{\infty} \sqrt{\frac{\beta_j x}{\tau'}} J_1(2\sqrt{\beta_j \tau' x}) e^{-\gamma\tau'} \times \cos[(\omega_{j+1} - \omega_j)\tau'] E(\tau - \tau', 0) d\tau', \quad (50)$$

which describes the propagation of a pulse with arbitrary temporal duration moving through a homogeneously broadened rigid-rotor medium.

To relate the physical significance of Eq. (50) to known results, one may for simplicity consider only a single resonance $j = 0 \rightarrow j = 1$. Applying Eq. (45) in Eq. (42) then yields

$$E(\omega, x) = \exp\left(-\frac{\beta_0 x}{i\omega - i\Delta\omega + \gamma} - \frac{\beta_0 x}{i\omega + i\Delta\omega + \gamma}\right) E(\omega, 0). \quad (51)$$

Furthermore, writing the electric field as a complex field plus its conjugate yields $E(\omega, x) = E^+(\omega, x) + E^-(\omega, x)$, where $E^+(\omega, x) = 0$ for $\omega < 0$ and $E^-(\omega, x) = 0$ for $\omega > 0$. Then, since $1/(i\omega + i\Delta\omega + \gamma) \approx 0$ for $\omega > 0$ in the sharp line limit, the solution for $E^+(\omega, x)$ is

$$E^+(\omega, x) = \exp\left(-\frac{\beta_0 x}{i\omega - i\Delta\omega + \gamma}\right) E^+(\omega, 0). \quad (52)$$

Equation (52) describes a 0π pulse in the frequency domain, a solution first derived by Crisp [50] [Eq. (21) in Crisp's paper]. Thus each j term in Eq. (50) represents a linear 0π pulse in the sharp line limit. The quantitative agreement between the two results is surprising, since the approximations that went into deriving Eqs. (50) and (52) are not the same as those of Crisp [50]. In particular, neither the rotating wave or slowly varying envelope approximations were made. The reason for the agreement is Eq. (45), which presumes that the resonances are narrow and spaced far apart. This emulates the mathematical behavior of the slowly varying envelope approximation and yields quantitative agreement between the two models. Note that for quasimonochromatic pulses propagating in two-level media the pulse area is traditionally defined as the area under the pulse envelope, but may also be defined as the Fourier coefficient on the resonance frequency. As envelopes are not used here we adhere to the latter definition; the 0π -pulse analogy appears due to the removal of the various molecular resonance frequencies from the initial pulse spectrum.

Arlt *et al.* [52] have derived analogous expressions to Eq. (50) under the slowly varying envelope and rotating wave approximations in the context of Rydberg wave packets. Equation (50) is a generalization of the results derived by Crisp [50] and Arlt *et al.* [52]; it represents a superposition of multiple single-cycle 0π pulses where each pulse is associated with an absorption line.

C. Impulse solution

Equation (50) is a general solution to the linearized sharp-line model. In the special case when $\beta_j = \beta$, the Bessel functions in Eq. (50) are always in phase and the integrand resonates when $\Delta\omega\tau' = k\pi$ where k is an integer. Pulse revivals may then be observed for $\tau \sim k\pi/\Delta\omega$. Under this simplification, the time-domain propagation dynamics can be described explicitly in terms of pulse revivals without the need for evaluating the convolution integral in Eq. (50).

First, observe that insertion of Eq. (40) in Eq. (41) and subsequent application of Eq. (45) yields

$$\partial_x E = - \sum_{j=0}^{J-1} \beta_j \int_{-\infty}^{\tau} E(\tau', x) e^{-\gamma(\tau-\tau')} \times (e^{i(\omega_{j+1}-\omega_j)(\tau-\tau')} + e^{-i(\omega_{j+1}-\omega_j)(\tau-\tau')}) d\tau', \quad (53)$$

in the time domain. To proceed further, we assume that $\beta_j = \beta = \text{constant}$, but remark that this equality does not hold in general. Under more realistic conditions, the populations are distributed according to a Maxwell-Boltzmann distribution, and the line intensities are then, evidently, not equal. The assumption $\beta_j = \beta$ is a crude approximation in the present context valid only closest to the interface $x = 0$ where the Bessel functions in Eq. (50) are small and have the same signs. However, by invoking this assumption, we obtain a compact, analytic solution that is convenient for understanding and illustrating the linear time-domain molecular response of the system, and its effect on the propagated pulse. This solution is included in the present report because Eq. (53) is generic for sharp-line, harmonic, multilevel systems for arbitrary pulse durations, and an analysis is relevant also in other physical contexts, most notably in multimode fiber Bragg

TABLE I. The x dependence of the driving pulse g_0 and the first five impulses.

$g_0(x)$	1
$g_1(x)$	$-(\alpha x)$
$g_2(x)$	$-(\alpha x) + \frac{1}{2}(\alpha x)^2$
$g_3(x)$	$-(\alpha x) + (\alpha x)^2 - \frac{1}{6}(\alpha x)^3$
$g_4(x)$	$-(\alpha x) + \frac{3}{2}(\alpha x)^2 - \frac{1}{2}(\alpha x)^3 + \frac{1}{24}(\alpha x)^4$
$g_5(x)$	$-(\alpha x) + 2(\alpha x)^2 - (\alpha x)^3 + \frac{1}{6}(\alpha x)^4 - \frac{1}{120}(\alpha x)^5$

grating transmission. Under the approximation $\beta_j \simeq \beta$, the model has only one length scale, substantially simplifying the analytic description of the spatial evolution. Equation (53) is written

$$\partial_x E = -\beta \int_{-\infty}^{\tau} E(\tau', x) \sum_{j=-J}^J e^{(j\Delta\omega - \gamma)(\tau - \tau')} d\tau'. \quad (54)$$

The $j = 0$ term included in Eq. (54) does not contribute to the integral unless E has a large dc component. When the spectrum of E lies within the rotational manifold, the limit $J \rightarrow \infty$ may be taken since the rapidly oscillating exponentials of the added terms average out under the time integration in Eq. (54). The sum is evaluated with Poisson resummation,

$$\sum_{j=-\infty}^{\infty} e^{j\Delta\omega(\tau - \tau')} = T_b \sum_{k=-\infty}^{\infty} \delta(\tau - \tau' - kT_b), \quad (55)$$

where $T_b = 2\pi/\Delta\omega$ is the quantum beat period of the system. Equation (54) evaluates to

$$\partial_x E(\tau, x) = -\frac{\alpha}{2} E(\tau, x) - \alpha \sum_{k=1}^{\infty} e^{-\gamma k T_b} E(\tau - kT_b, x), \quad (56)$$

where $\alpha = \beta T_b$ is the reciprocal characteristic length scale. Equation (56) is solved exactly with the ansatz

$$E(\tau, x) = \sum_{k=0}^{\infty} g_k(x) e^{-\alpha x/2 - \gamma k T_b} E(\tau - kT_b, 0), \quad (57)$$

where $E(\tau - kT_b, 0)$ is the input pulse shifted an amount kT_b in time. Substituting Eq. (57) into Eq. (56) yields a recursive equation for the unknown algebraic factors $g_k(x)$:

$$\partial_x g_k(x) = -\alpha \sum_{l=0}^{k-1} g_l(x). \quad (58)$$

The boundary condition on $x = 0$ yields $g_0 = 1$; remaining terms are found by recursive integration. The first few factors g_k are summarized in Table I.

Equation (57) shows that the pulse evolves into a series of impulses following the driving pulse ($k = 0$), which decays exponentially with propagation distance. The result is interpreted as follows. As the pulse enters into the material, it excites a coherent superposition of molecular eigenstates in the material (i.e., a rotational wave packet), which oscillates freely in the absence of the pulse. Due to the harmonic spacing of the energy levels and equal line intensities, the rotational wave packet rephases at times $\tau = kT_b$ and emits radiation. Under idealized conditions, dispersive broadening cancels and the

emitted radiation is a temporal copy of the input pulse, delayed a time kT_b and homogeneously dampened by a factor $e^{-\gamma k T_b}$. The inequality $\gamma T_b \ll 1$ is satisfied for a wide class of media (e.g., the hydrogen halides) and the pulse train described by Eq. (57) may be very long. According to Eq. (42), the pulse spectrum resembles an inverse frequency comb. In optically thin materials $\alpha x \ll 1$, the impulses have the same amplitude and are π radians out of phase with the driving field, and have been termed commensurate THz echoes [24,25] in the context of terahertz excitation.

IV. NUMERICAL METHOD

We now turn our attention to the numerical algorithm used to solve the RMB equations. This algorithm implements standard differential methods and is thus of little mathematical interest, but the application of these techniques to the multi-level RMB equations is a signification extension of existing pulse propagation algorithms [27–34,53], and is therefore discussed in detail here. Our computational method for the optical Bloch equations is quite general and follows that due to Bidégaray *et al.* [31] and Marskar and Österberg [34] where matrix methods were used to solve for multilevel media. These techniques are readily adapted to other kinds of multilevel systems, including homogeneously and inhomogeneously broadened media [34]. The propagation equation is solved with the implicit trapezoidal rule.

Note that the total number of rotational states in a rigid-rotor molecule truncated at $j = J$ is $(J + 1)^2$, and the dimension of the density operator is therefore $(J + 1)^4$. Thus truncation at $J = 87$ gives a total of 7744 rotational eigenstates, and the system is represented by roughly 60 million parametrically coupled partial differential equations that must be solved for in $(1 + 1)$ dimensions. This problem is of substantial complexity in a pulse propagation context. Presently, reported computer solutions of coherent single-cycle pulse propagation have only been presented for a few levels [30,34,43,54,55].

A. Subspace formulation

Recall that for linearly polarized fields the interaction term $\mu \cdot E$ is nonzero only for transitions $j \rightarrow j \pm 1$, $m \rightarrow m$. Arranging the state vector $|\Psi\rangle$ in order of largest negative m to largest positive m , and from smallest to largest j , the z component of the dipole moment operator is

$$\mu = \begin{pmatrix} \overbrace{(0)}^{m=-J} \\ \underbrace{\begin{pmatrix} 0 & \mu_{J-1, Jm} \\ \mu_{Jm, J-1m} & 0 \end{pmatrix}}^{m=-J+1} \\ \vdots \\ \underbrace{(0)}^{m=J} \end{pmatrix} = \bigoplus_{m=-J}^{m=J} \mu^{(m)}, \quad (59)$$

where $\mu^{(m)}$ is a $(J - |m| + 1) \times (J - |m| + 1)$ dimensional Hermitian matrix. Empty entries in Eq. (59) are filled with zeros. Equation (59) defines a block diagonal matrix with entries $\mu^{(m)}$, where \bigoplus is the direct matrix sum. For initial states without coherence between different m levels, the density operator and the free Hamiltonian share the same sparsity and also decompose as block diagonal matrices,

$$H_0 = \bigoplus_{m=-J}^{m=J} H_0^{(m)}, \quad (60a)$$

$$\rho = \bigoplus_{m=-J}^{m=J} \rho^{(m)}. \quad (60b)$$

Multiplication between block diagonal matrices yields

$$\left(\bigoplus_m O_1^{(m)} \right) \left(\bigoplus_m O_2^{(m)} \right) = \bigoplus_m O_1^{(m)} O_2^{(m)}, \quad (61)$$

where $O_1^{(m)} O_2^{(m)}$ is a normal matrix product. This property allows the von Neumann equation to be solved in terms of each block m ,

$$i\hbar\rho^{(m)} = [H_0^{(m)} - E\mu^{(m)}, \rho^{(m)}]. \quad (62)$$

Equation (62) is an exact decomposition of Eq. (13) for linearly polarized fields in the coherent regime. The physical interpretation of the decomposition into partial contributions is straightforward. Since the molecules are initially distributed over all azimuthal rotational modes (m modes) but no coherence can be established between these, we may decompose the density operator into each subspace m and solve only for the θ -motion of each mode, leaving the φ rotations as frozen variables incorporated into the initial conditions of ρ . This process reduces the $(J + 1)^2 \times (J + 1)^2$ -dimensional density operator into $2J + 1$ partial density operators $\rho^{(m)}$ with dimensions $(J - |m| + 1) \times (J - |m| + 1)$, each of which describe the θ motion of the molecule for a given azimuthal rotational mode. The largest partial density operator is $\rho^{(0)}$, which has dimension $(J + 1) \times (J + 1)$, which for large J is substantially smaller than the full operator. The initial population in the $|Jm = \pm J\rangle$ states is not coupled to other states, and $\rho^{(-J)}$ and $\rho^{(J)}$ are constant matrices of dimension 1×1 .

The number of nonzero entries in the decomposed density operator is comparatively large. For example, for $J = 87$, there are 459,448 nonzero elements in ρ . Thus, even sparse numerical storage of ρ is both time consuming and resource exhaustive, necessitating calculation of relevant observables during run time. These are calculated on each subspace m ,

$$\text{Tr}(O_1 O_2) = \text{Tr} \left(\bigoplus_{m=-J}^{m=J} O_1^{(m)} O_2^{(m)} \right) = \sum_{m=-J}^{m=J} \text{Tr}(O_1^{(m)} O_2^{(m)}). \quad (63)$$

Equation (63) allows calculations in terms of partial operators instead of full ones, avoiding the need for large matrix

multiplications. In the same way, Eq. (26) becomes

$$\varrho(\tau, x; \theta) = \sum_{m=-J}^J \rho^{(m)}(\tau, x) : G^{(m)}(\theta), \quad (64)$$

where $G^{(m)}(\theta)$ is a $(J - |m| + 1) \times (J - |m| + 1)$ -dimensional matrix with entries

$$G_{k,k'}^{(m)}(\theta) = Y_{|m|+k-1}^m(\theta, \varphi) Y_{|m|+k'-1}^{m*}(\theta, \varphi), \quad (65)$$

where $k, k' \in [1, J - |m| + 1]$. An analogous expression is found for $L^{(m)}$ describing the Legendre moments.

B. Discretization

The RMB equations are solved numerically by using an implicit trapezoidal method for Eq. (8) and an operator splitting method for Eq. (62). To avoid accumulation of numerical round-off errors, E and μ are first normalized by characteristic values E_c and μ_p such that they are of order one. We introduce the characteristic time scale τ_c as the reciprocal Rabi frequency $\tau_c = \hbar/(E_c\mu_p)$, and a characteristic length scale $l_c = 2c\tau_c\epsilon_0 E_c/(\mathcal{N}\mu_p)$. With this specification, Eqs. (8) and (62) become

$$\frac{\partial \Omega}{\partial \xi} = i \text{Tr}(v[\mathcal{H}_0, \rho]), \quad (66a)$$

$$\frac{d\rho^{(m)}}{d\eta} = -i[\mathcal{H}_0^{(m)}, \rho^{(m)}] + i\Omega[v^{(m)}, \rho^{(m)}]. \quad (66b)$$

All quantities in Eq. (66) are dimensionless and of order one with $E/E_c \rightarrow \Omega$, $\tau/\tau_c \rightarrow \eta$, $x/l_c \rightarrow \xi$, $H_0\tau_c/\hbar \rightarrow \mathcal{H}_0$, $\mu/\mu_p \rightarrow v$. The density operator ρ is already dimensionless and of order unity and is unaffected. The right-hand side of Eq. (66a) is obtained from

$$\frac{d}{d\tau} \text{Tr}(\mu\rho) = \frac{-i}{\hbar} \text{Tr}(\mu[H_0 - \mu E, \rho]) = \frac{-i}{\hbar} \text{Tr}(\mu[H_0, \rho]), \quad (67)$$

where $\text{Tr}(\mu[\mu, \rho]) = 0$ by the cyclic permutation invariance of the trace operation.

1. Propagation equation

An implicit trapezoidal (i.e., the second-order Adams-Moulton) method is used for solving Eq. (66a):

$$\Omega_{i+1}^{n+1} = \Omega_i^{n+1} + \frac{i\Delta\xi}{2} \text{Tr}(v[\mathcal{H}_0, \rho_{i+1}^{n+1} + \rho_i^{n+1}]). \quad (68)$$

Following Eq. (63), the trace of the term containing the full density operator on the right-hand side of Eq. (68) is written as a reduction over the subspaces,

$$\text{Tr}(v[\mathcal{H}_0, \rho]) = \sum_{m=-J}^{m=J} \text{Tr}(v^{(m)}[\mathcal{H}_0^{(m)}, \rho^{(m)}]). \quad (69)$$

2. Bloch equations

The evolution of ρ is spatially local and co-located spatial and temporal grids for ρ and Ω are used. An important property of the numerical solution to the coupled system is that the time evolution of ρ is unitary. To ensure this, a second-order

approximate form of the exact solution to Eq. (66b) over increment $\Delta\eta$ is used. The approximate solution to Eq. (66b) in the interaction picture is

$$\rho_I^{(m)}(\Delta\eta) = U_I(\Delta\eta)\rho_I^{(m)}(0)U_I^\dagger(\Delta\eta), \quad (70)$$

where

$$U_I^{(m)}(\Delta\eta) = \exp\left[i\int_0^{\Delta\eta}\mathcal{H}_I^{(m)}(\eta)d\eta\right], \quad (71)$$

and $\rho_I^{(m)}$ and $\mathcal{H}_I^{(m)}$ are the corresponding density and Hamiltonian operators in the interaction picture of subspace m . The free and interaction propagators in this subspace are denoted by $U_0^{(m)}$ and $U_I^{(m)}$, respectively. In arriving at Eq. (70) we have expanded the time-ordered interaction propagator in its Magnus series and truncated this series at the first term under the assumption that the time step $\Delta\eta$ is sufficiently small. The interaction Hamiltonian $\mathcal{H}_I^{(m)}(\eta) = \Omega(\eta)U_0^{(m)\dagger}v^{(m)}U_0^{(m)}$ is approximated $\mathcal{H}_I^{(m)}(\eta) \approx \Omega(\eta)v^{(m)}$ to the same order. The integral in Eq. (70) is approximated as $\int_0^{\Delta\eta}\mathcal{H}_I^{(m)}(\eta)d\eta \approx v^{(m)}(\Omega^{n+1} + \Omega^n)\Delta\eta/2$. By approximating the interaction matrix exponentials $U_I \equiv \exp(2i\mathbb{C}) \approx (1 - i\mathbb{C})^{-1}(1 + i\mathbb{C})$ and by using a Strang splitting $U_0U_I \approx U_0^{1/2}U_IU_0^{1/2}$, the final discretized form of Eq. (70) used in this paper is

$$\rho_{i+1}^{(m)n+1} = \mathbb{F}_m(\mathbb{N}_m^{-1})^\dagger \mathbb{N}_m \mathbb{F}_m \rho_{i+1}^{(m)n} \mathbb{F}_m^\dagger \mathbb{N}_m^\dagger \mathbb{N}_m^{-1} \mathbb{F}_m^\dagger. \quad (72)$$

The linear (\mathbb{F}_m) and nonlinear (\mathbb{N}_m) propagators in Eq. (72) are defined as

$$\mathbb{F}_m = \exp\left(-\frac{i\mathcal{H}_0^{(m)}\Delta\eta}{2}\right), \quad (73)$$

$$\mathbb{N}_m = 1 + iv^{(m)}\frac{(\Omega_{i+1}^{n+1} + \Omega_{i+1}^n)\Delta\eta}{4}. \quad (74)$$

In Eq. (72), we have used $(1 - i\mathbb{C})^{-1} = [(1 + i\mathbb{C})^{-1}]^\dagger$ since $\mathbb{C} \equiv v^{(m)}(\Omega_{i+1}^{n+1} + \Omega_{i+1}^n)\Delta\eta/4$ is Hermitian. Unitarity of $U_I^{(m)}$ follows by $U_I^{(m)}U_I^{(m)\dagger} = 1$. The free propagators \mathbb{F}_m are constant and are calculated exactly since $\mathcal{H}_0^{(m)}$ is diagonal. The inverse matrices \mathbb{N}_m^{-1} must be found using numerical calculations. In this paper, they are calculated by using an LU factorization $\mathbb{N}_m^{-1} = (\mathbb{L}_m\mathbb{U}_m)^{-1} = \mathbb{U}_m^{-1}\mathbb{L}_m^{-1}$. We point out that Crank-Nicholson-type discretizations of Eq. (62), which are frequently used for two-level materials [27] have positiveness issues [31] and are not appropriate when more than two levels are involved. In contrast, Eq. (72) is valid for arbitrary Bloch dimensions and is absolutely stable for any value of $\Delta\eta$.

The unknown quantities Ω_{i+1}^{n+1} and $\rho_{i+1}^{(m)n+1}$ entering into the right-hand sides of both Eqs. (68) and (72) prevent direct inversion of the discretized equations of motion. To overcome this, Eqs. (68) and (72) are solved by using an iterative predictor-corrector method. The predicted values for Ω_{i+1}^{n+1} and $\rho_{i+1}^{(m)n+1}$ are supplied by approximating $\Omega_{i+1}^{n+1} \approx \Omega_{i+1}^n$ and $\rho_{i+1}^{(m)n+1} \approx \rho_i^{(m)n+1}$ in the right-hand sides of Eqs. (68) and (73). These values are then replaced into the right-hand sides of the same equations to gain new values for the unknowns Ω_{i+1}^{n+1} and $\rho_{i+1}^{(m)n+1}$, and the process is iterated until a convergence criteria is met.

TABLE II. Parameters used for computer simulations.

Variable	Symbol	Value
Number density	\mathcal{N}	10^{18} cm^{-3}
Quantum beat period	T_b	5 ps
Permanent dipole moment	μ_p	$5 \times 10^{-29} \text{ Cm}$
Energy levels	$J + 1$	88
Rotational eigenstates	$(J + 1)^2$	7744
Density matrix dimension	$(J + 1)^2 \times (J + 1)^2$	7744×7744
Propagation length	L	10 cm

3. Parallelization and performance

The most expensive parts of the numerical evaluation of Eqs. (68) and (72) are the matrix inversion and multiplications required for updating Eq. (72). These parts are optimized by performing the matrix product $\mathbb{G}_m = \mathbb{F}_m \rho_{i+1}^{(m)n} \mathbb{F}_m^\dagger$ element-wise since \mathbb{F}_m is diagonal. These calculations are moved outside the correction loop since \mathbb{G}_m only needs to be calculated once per (i, n) . In the same way, $\mathbb{N}_m \mathbb{G}_m \mathbb{N}_m^\dagger = \mathbb{G}_m + ia[v^{(m)}, \mathbb{G}_m] + a^2 v^{(m)} \mathbb{G}_m v^{(m)}$ with $a \equiv (\Omega_{i+1}^{n+1} + \Omega_{i+1}^n)\Delta\eta/4$ allows the matrix multiplications to be moved outside the correction loop, leaving a scalar update of the individual elements based on the predicted value of Ω_{i+1}^{n+1} . Optimized sparse matrix routines are used for performing the matrix multiplications since \mathbb{F}_m and $\hat{v}^{(m)}$ are sparse (diagonal and tridiagonal) matrices. If necessary, which would only be the case for very large values of J , the remaining part of the algorithm (i.e., finding and multiplying with \mathbb{N}_m^{-1}) can be parallelized by using standard parallel linear algebra libraries.

Our experience is that serial codes that solve for the full density operator are feasible for $J \lesssim 10$ if sparse matrix multiplications are used, and that parallel codes are otherwise required. Our code is parallelized by distributing the $2J + 1$ subspaces [56] over an equal number of processes by using the message passing interface (MPI). The run time is determined by the serial execution time of the largest subspace, which is of dimension $(J + 1)$. Using $J = 87$ on a 500×1000 grid, giving a total of 7744 eigenstates, our code executes in less than a few hours on a SGI Altix ICE X cluster with two 8-core Intel Sandy Bridge (2.6 GHz) processors on each node. We have also developed codes that solve for the full $(J + 1)^2 \times (J + 1)^2$ -dimensional density operator using distributed matrix inversion and multiplication methods, but these codes perform significantly slower than the subspace method above. However, such codes solve for the full density operator and are useful for elliptically polarized fields where subspace decomposition is not possible.

C. Comparison with analytic solutions

To mutually verify the reliability of our analytic results and numerical method, we now compare the analytic solutions with the results of computer simulations. Our choice of parameters is summarized in Table II; the numbers do not represent a particular medium.

The unidirectional and linear approximations are well satisfied for our chosen parameters: we find, for example, $P/(\epsilon_0 E_0) \sim 10^{-2}$ [see Fig. 4(b)], and this is the case for all

of our computer simulations. The “infinite-ladder” approximation used in Eq. (55) is satisfied since the highest-lying molecular transition $\omega_J - \omega_{J-1} \sim 10^{14}$ rad/s lies well outside of the input pulse spectrum.

1. Choice of input pulse

Since the zero-frequency wave component radiated by a finite-size source propagates evanescently, a basic propagation requirement prior to reaching the medium is that the zero-frequency (dc) Fourier coefficient of the input pulse is zero [44,57]. While this is not obvious from the plane-wave equation (1), a simple and clear argument for this requirement may be provided by considering the three-dimensional wave equation

$$\left(\nabla^2 - \frac{1}{c} \frac{\partial^2}{\partial t^2}\right) E(t, \mathbf{r}) = 0, \quad (75)$$

which has a solution $E = E_0 e^{i\mathbf{k}\cdot\mathbf{r} - i\omega t}$ with $k_x = \sqrt{\omega^2 - k_\perp^2}$, where k_\perp is the transverse wave number. The propagation constant of the dc Fourier coefficient is then $k_x = ik_\perp$, which represents a nonoscillating, nonpropagating field. In particular, such fields may only be established over the length of the medium by placing an appropriate electric charge distribution a finite distance away from it. This implies that if the pulse source consists of an aperture with transverse width R , for which $k_\perp \sim 1/R$, dc fields are localized to the vicinity $x \sim R$. For distances $x \gg R$, which represents the most common experiments, the dc field vanishes and thus we require that $\int_{-\infty}^{\infty} E(\tau, 0) d\tau = 0$. For this reason we reject the use of, e.g., Gaussian pulses where the dc Fourier coefficient depends strongly on the carrier-envelope phase in the single-cycle regime [35]. Instead, we apply a Poisson input pulse [58],

$$E(\tau, 0) = \frac{1}{2} E_0 e^{i\phi} \left(1 - \frac{i\omega_c \tau}{s}\right)^{-(s+1)} + \text{c.c.} \quad (76)$$

The parameters s , ω_c , and ϕ describe the pulse duration, location of the spectral peak, and the spectral phase, respectively. The pulse described by Eq. (76) has a vanishing zero-frequency component, and is symmetric with respect to $\tau = 0$ for $\phi = 0$ and antisymmetric for $\phi = \pi/2$. For s close to unity, Eq. (76) describes a single-cycle pulse; for large s , the limiting form of Eq. (76) is a Gaussian pulse with carrier frequency ω_c , carrier-envelope phase ϕ , and duration $T = \sqrt{2s}/\omega_c$. Pulse chirping may be taken into account by treating ω_c as a complex parameter [58]. In this section, we take $E_0 = 5 \times 10^6$ V/m, $\phi = \pi/2$, $s = 3$, and $\omega_c = 3\pi \times 10^{12}$ rad/s. This choice of parameters represents an asymmetric single-cycle pulse consisting of two main “carrier lobes” where the leading oscillation is parallel with the z axis ($\mathbf{z} \cdot \mathbf{E} > 0$), and the trailing oscillation is antiparallel ($\mathbf{z} \cdot \mathbf{E} < 0$). Taking the Fourier transform of Eq. (76) gives

$$E(\omega, 0) = 2\pi E_0 e^{i\phi} \left(\frac{s}{\omega_c}\right)^{s+1} \frac{\omega^s e^{-s\omega/\omega_c}}{\Gamma(s+1)} u(\omega) + 2\pi E_0 e^{-i\phi} \left(\frac{s}{\omega_c}\right)^{s+1} \frac{(-\omega)^s e^{s\omega/\omega_c}}{\Gamma(s+1)} u(-\omega), \quad (77)$$

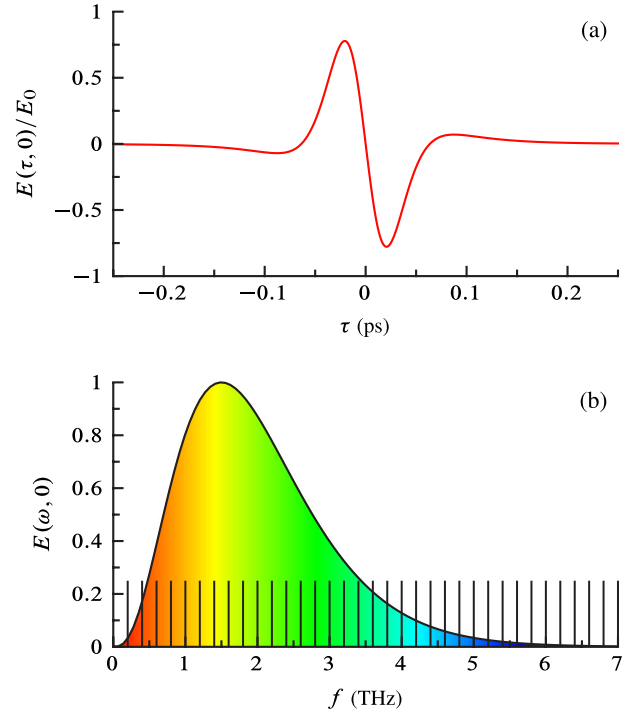


FIG. 3. (Color online) (a) Input pulse $E(\tau, 0)$ in units of E_0 . (b) Normalized input spectrum $E(\omega, 0)$. The vertical bars near the baseline indicate the spectral position of the first few absorption lines, which extend up to approximately 17.5 THz.

where Γ is the Gamma factorial function and $u(\omega)$ the unit step function in the frequency domain. With the parameters above, Eq. (76) describes a spectrum that peaks at 1.5 THz and extends up to approximately 5 THz. For comparison, with $J = 87$ the transition frequency of the highest-lying transition is roughly 17.5 THz. The input pulse in the time and frequency domains is shown in Fig. 3.

2. Impulse solution

First, we consider linear interactions under the condition of equal line strengths. With the above choice of parameters, we fix the initial rotational state distribution such that the first 63 rotational absorption lines have the same intensity, which yields an optical thickness $\alpha L \approx 9$. Figure 4(a) shows the spatial evolution of the input pulse for the first three quantum beat periods. According to Eq. (57), the driving pulse is followed by a sequence of impulses propagating at the vacuum light velocity spaced exactly one quantum beat period apart, features that are captured in our computer simulation. Figure 4(b) shows the near single-cycle pulse close to the interface at $x \gtrsim 0$, and also the molecular orientation $\langle \cos \theta \rangle$ at the same position; the expected rotational wave packet revivals are readily observed as recurring orientations at every $\tau = kT_b$. The angular distribution achieved at these intensities is only slightly perturbed from the isotropic distribution since $\langle \cos \theta \rangle \sim 10^{-3}$, indicating very weak molecular orientation. Furthermore, we briefly mention that the results in Fig. 4(b) may be compared favorably with the computer simulations by Fleischer *et al.* [7] [see Figs. 2(b) and 3(a)].

To examine the pulse evolution in greater detail, we compare in Fig. 5 the computer solution with the analytic

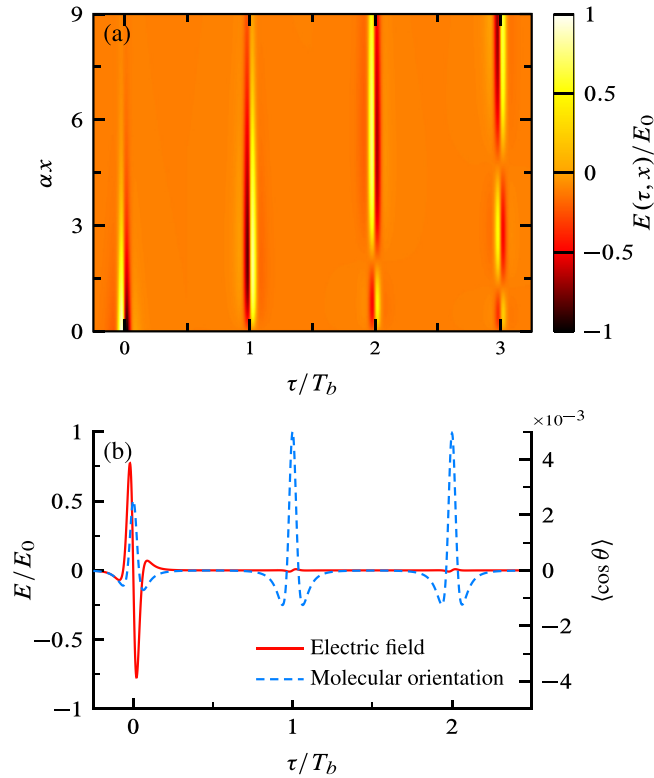


FIG. 4. (Color online) Numerical solution using the Poisson input pulse (76) under the “equal line strength” simplification. (a) Spatiotemporal evolution of $E(\tau, x)$. (b) Temporal evolution of the electric field (solid line) in units of E_0 and the molecular orientation $\langle \cos \theta \rangle$ (dashed line, plotted against the right vertical axis) at the entrance interface.

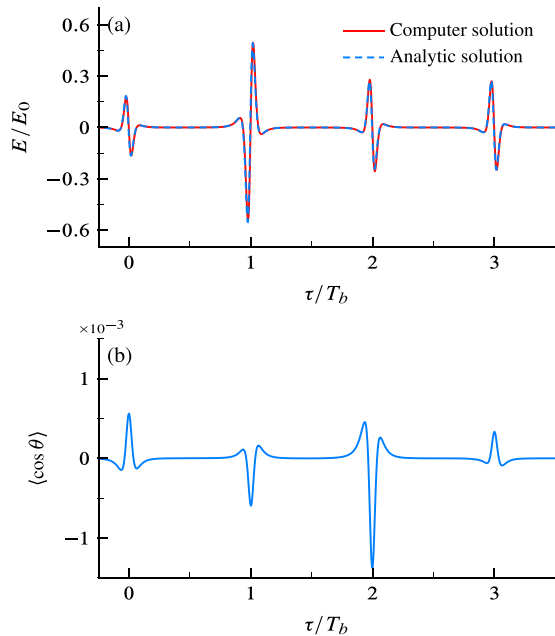


FIG. 5. (Color online) Numerical solution under the “equal line strength” simplification. (a) Comparison between the computer solution (solid line) and the analytic solution (57) (dashed line) after a propagation distance $\alpha x = 3$. (b) Computer solution showing the temporal evolution of the orientation at $\alpha x = 3$.

solution (57) after the pulse has propagated an optical distance $\alpha x = 3$. The solid line in Fig. 5(a) shows the computer solution for the electric field, with revivals occurring at each rephasing period $\tau = kT_b$. The amplitudes of the impulses in the computer solution are in excellent agreement with the predictions of the analytic impulse solution and leave no doubt about the reliability of our computer simulations. Correspondingly, Fig. 5(b) shows the temporal evolution of the orientation $\langle \cos \theta \rangle$ for the same computer simulation. We find that the peak orientation is smaller than at the entrance interface, which is due to absorption of the various resonance frequencies over the first few Beer lengths. In effect, after a few Beer’s lengths into the medium, the initial resonant frequency content is cut out of the pulse spectrum, and the molecules are excited nonresonantly and therefore less orientated than at the entrance interface. A propagation-induced phase reversal of the orientation is also observed. The phase difference of the first orientational revival at $\alpha x = 0$ and $\alpha x = 3$ is precisely π .

In the coherent regime, the polarization and the electric field are occasionally antiparallel. Examination of Fig. 4(b) shows that at the trailing edge of the input pulse, $\langle \cos \theta \rangle < 0$ and $E > 0$. To emphasize this, consider the polarization P [recall Eq. (56)] after the resummation:

$$P(\tau, x) = \alpha \epsilon_0 c \int_{-\infty}^{\tau} E(\tau', x) + 2 \sum_{k=1}^{\infty} E(\tau' - kT_b, x) d\tau', \quad (78)$$

which shows that the polarization does not in general follow the instantaneous electric field, as is expected this close to resonance. From Eq. (78), we observe also that the orientational revivals have (i) twice the amplitude of the initial field-induced orientation and (ii) are temporally separated only for pulse durations shorter than T_b . Both features are clearly present in Fig. 4(b). These features have been observed also by other through computer simulations (see, e.g., Fleischer *et al.* [7]), but have, to the best of our knowledge, not been explained. At the interface $x = 0$ for times $\tau < T_b/2$, the molecules are oriented quasistatically by the pulse:

$$P(\tau, 0) = \alpha \epsilon_0 c \int_{-\infty}^{\tau} E(\tau', 0) d\tau'. \quad (79)$$

Close to the leading edge of the driving pulse in Fig. 4(b) where the field is positive, $\langle \cos \theta \rangle$ is also positive and the polarization is parallel with the electric field. The rotors remain parallel until the electric field switches polarity, and the molecules become oriented opposite to the external field. In comparison to molecular alignment using static electric fields, this result is counterintuitive and warrants an explanation. It suffices to consider a classical dielectric response $P(\omega) = \chi(\omega)E(\omega)$ where $\chi(\omega) = \chi^*(-\omega)$. For an isolated quantum Lorentz resonance,

$$\chi(\omega) = \chi_0 \left(\frac{1}{\omega_0 - \omega} + \frac{1}{\omega_0 + \omega} \right), \quad (80)$$

$P(\tau)$ evaluates to $P(\tau) = \chi_0 \int_{-\infty}^{\tau} \sin[\omega_0(\tau - \tau')] E(\tau') d\tau'$ and the medium responds only at the resonance frequency ω_0 . When $E(\omega)$ overlaps with ω_0 and has a spectral bandwidth exceeding the absorption linewidth by orders of magnitude, the

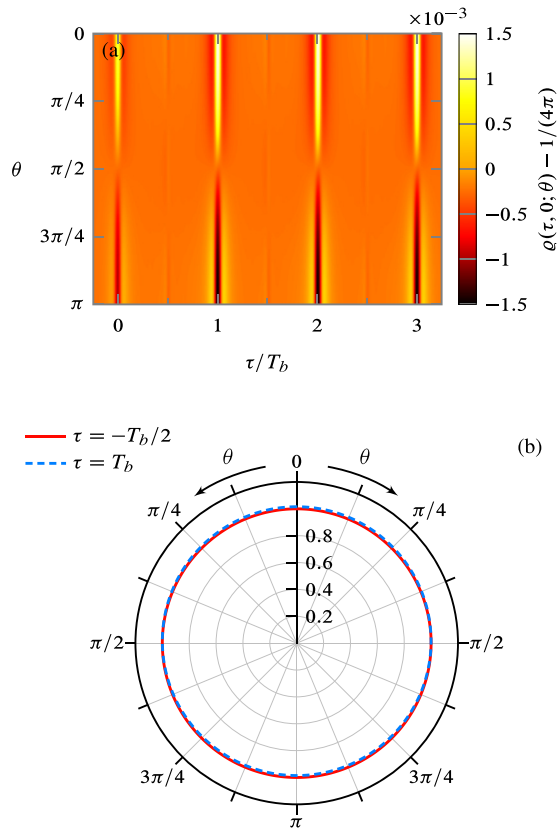


FIG. 6. (Color online) Computer solution for the molecular probability density at the entrance interface under the “equal line strength” simplification. (a) The values for the color-coded data indicate the displacement from the isotropic distribution. (b) Cross section of the probability density through the polar plane for times $\tau = -T_b/2$ (solid) and $\tau = T_b$ (dashed). The distance from the origin indicates the value of ϱ in multiples of $1/(4\pi)$.

pulse may reverse polarity faster than the medium can follow. This manifests itself as antiparallel electric and polarization field vectors, opening up the possibility of a radiation reaction that transfers energy back to the pulse. This effect has been known for a long time, and is the primary mechanism for the optical transparency of the linear 0π pulse in the zero damping limit, first predicted by Crisp [50] and later observed by Varoquaux [59] and Rothenberg [60]. In essence, Eq. (57) is the multilevel superposition of linear 0π pulses when the absorption coefficients associated with each rotor transition are equal. The quantum beats at time delays that are integer multiples of T_b are manifestations of coherent beating between these pulses.

Figures 6(a) and 6(b) show the probability density in the linear interaction regime close to the entrance interface. At the isochronic line $\tau = -T_b/2$, the probability density is constant $\varrho = 1/(4\pi)$ and the molecular axes are distributed isotropically over the unit sphere. Moving towards $\tau \sim 0$ the rotor molecules are quasistatically lining up with the leading lobe of the external THz pulse, manifesting as a slight increase in the probability density on the northern hemisphere. After the pulse has passed, the molecules dephase in the absence of the external field and the orientation diminishes.

When $\tau \rightarrow T_b$ the first wave-packet revival is observed as an increased probability density at the northern hemisphere $\theta = 0$ and a decreased density at $\theta = \pi$. This process repeats itself for longer times resulting in the re-emergence of an oriented molecular ensembles at times kT_b . Note that at half integer revival times $\tau = (k + 1/2)T_b$ then $\langle \cos \theta \rangle = 0$ but $\langle \cos^2 \theta \rangle_c \neq 0$. For the simulation data in Fig. 6, we find $\langle \cos \theta \rangle \approx 0$ and $\langle \cos^2 \theta \rangle_c \sim 10^{-4}$ at $\tau = T_b/2$. The molecules are therefore weakly aligned, but not oriented, at half-quantum beat periods.

Although the molecules reorient at each integer quantum beat period the rotor molecules are only slightly perturbed. Figure 6(b) shows a detailed cross section of ϱ through the molecular polar plane for two different times $\tau = -T_b/2$ (solid line) and $\tau = T_b$ (dashed line). The lines are plotted for the entire polar cross section with the understanding that the probability density is symmetric with respect to $\theta \rightarrow 2\pi - \theta$. The radial distance from the origin to the two curves indicates the value of ϱ in each case. By integrating figures like Fig. 6(b), we have verified that probability is conserved in our simulations to a precision better than 10^{-5} .

3. Initial thermal equilibrium

Next, we consider media in thermal equilibrium where the initial state of the medium prior to the action of the pulse is

$$\rho(\tau \rightarrow -\infty, x) = \frac{1}{Z} \exp\left(-\frac{H_0}{k_B T}\right), \quad (81)$$

where $Z = \text{Tr}(\exp[-H_0/(k_B T)])$ is the partition function. With this choice of parameters, the most populated rotational level is $j = 5$ where $\rho_{5m,m} \approx 0.01$. The line intensities associated with each $j \rightarrow j + 1$ transition are evidently different in the thermal and idealized cases. We now consider propagation of the same input pulse as used above, but now through a medium in thermal equilibrium at $T = 300$ K. Analogous to Fig. 4(a), Fig. 7 shows the spatiotemporal evolution of $E(\tau, x)$ over the first two quantum beat periods for the entire length of the medium. Close to the entrance interface, wave packet revivals are observed at each time $\tau = kT_b$ as expected from the linear analysis. However, as the driving pulse and impulses propagate further into the material, the roles of the Bessel factors in Eq. (50) become noticeable and the pulse revivals begin to disperse. Evidently, close to the interface, the Bessel functions in Eq. (50) may be expanded in a power series and the integrand resonates at $\tau' = 2\pi/(\Delta\omega)$ since all $\beta_j x$ are comparatively small with respect to the first abscissa of the Bessel function such that $J_1(2\sqrt{\beta_j \tau' x}) > 0$. Following Eq. (46), dispersion is therefore negligible for optically thin media $\beta_j x \ll 1$. After a sufficient propagation length where the Bessel factors with the largest β_j change from positive to negative, the phases of the polarization components associated with the strongest absorption lines are reversed relative to the weaker lines. Thus, when the driving pulse has penetrated a sufficient distance into the material, the various rigid-rotor transitions are, due to different level degeneracies and populations, excited with different amplitudes and phases. As the first impulse is emitted close to the interface, it effectively enters into a medium predominantly prepared by excitation of the strongest resonance lines. This impulse, which

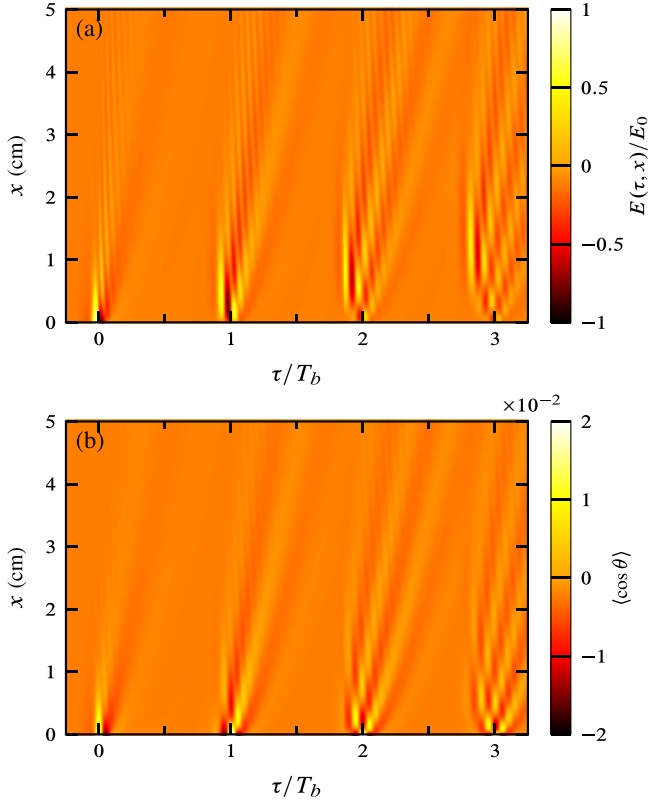


FIG. 7. (Color online) Computer solution for single-cycle pulse THz excitation of a molecular ensemble in initial thermal equilibrium. The color-coded data in (a) and (b) show the electric field $E(\tau, x)/E_0$ and the molecular orientation $\langle \cos \theta \rangle$, respectively.

is approximately a copy of the initial pulse, reinforces this response for the later impulses, leading to additional dephasing among the various polarization components. In the spectral domain, an equivalent description is that spectral holes are only found at the strongest absorption lines during propagation, and the pulse develops a more complicated temporal structure. Note that molecular dephasing of rotational wave packets due to centrifugal distortion of the molecule for higher rotational modes has been discussed by Harde *et al.* [24]. Here, we show that for an extended medium, dephasing also occurs as a result of dispersive propagation.

Figure 7(b) shows the value of $\langle \cos \theta \rangle$ for the entire simulation region and demonstrates the corresponding dispersion of the induced molecular orientation. Like the pulse, recurring periods of orientation are found at times $\tau = kT_b$ close to the entrance interface. As above, the propagation-induced dispersion of the rotational wave packet becomes noticeable for longer propagation lengths, and manifests as temporal broadening of the orientational revivals.

V. NONLINEAR PROPAGATION

Having discussed the linear pulse propagation regime, we now turn our attention to nonlinear propagation. Below, we consider three cases $E_0 = 10^8, 10^9$, and 5×10^9 V/m. In each case, the medium is initially prepared as a thermal ensemble following Eq. (81) with $T = 300$ K as above.

TABLE III. Normalized pulse areas for the $j=5 \rightarrow j=6$ ($m=0$) transition using different pulse amplitudes. The medium is initially in thermal equilibrium at 300 K.

Nonlinear Regime	E_0	Pulse area Θ_j^m
Weak	10^8 V/m	≈ 0.6
Intermediate	10^9 V/m	≈ 60
Strong	5×10^9 V/m	≈ 1500

The violation of the linear approximation may be estimated by evaluating the pulse area Θ_j^m [Eq. (39)] for the above choice of parameters. Recall that the most populated level is initially $j=5$, and that $\rho_{jm, jm} - \rho_{j+1m, j+1m} \approx 0.0018$ for the $j=5 \rightarrow j=6$ transition. The pulse duration may be taken as roughly $T \approx 130$ fs, which is the distance between the two zero-crossings of the main lobes; the transition dipole moment is roughly $\mu_{jm, j+1m} \approx 0.5\mu_p$ for $m=0$. Table III summarizes the numerical evaluation of Θ_j^m for the three pulse amplitudes mentioned above. We divide, loosely speaking, the interaction regime into three regimes corresponding to the cases $\Theta_j^m \sim 1$, $\Theta_j^m > 1$, and $\Theta_j^m \gg 1$, respectively.

Finally, we briefly mention that practical limitations prevent us from propagating pulses with even higher amplitudes since (i) the time scale $\tau_c < 1$ fs implies a very fine temporal resolution and (ii) population is then excited to $j=J$, which invalidates the finite numerical truncation of accessible rigid-rotor states. Note, nonetheless, that the chosen dipole moment μ_p is comparatively large, and that the numerical results are therefore applicable for even higher field strengths in molecules with smaller dipole moments.

A. Weakly nonlinear regime $\Theta_j^m \sim 1$

First, we investigate the propagation of a pulse with amplitude $E_0 = 10^8$ V/m, which yields $\Theta_5^0 \approx 0.6$. The corresponding pulse intensity is $I_0 = \epsilon_0 c |E_0|^2 / 2 = 1.32$ GW/cm². Figure 8 shows the j -level population distribution

$$w_j(\tau, x) = \sum_{m=-j}^j \rho_{jm, jm}(\tau, x) \quad (82)$$

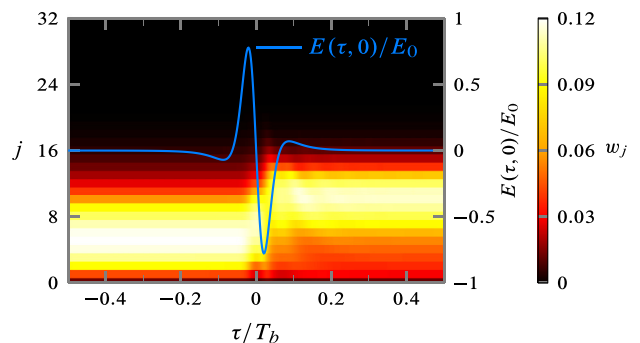


FIG. 8. (Color online) $\Theta_j^m \sim 1$: rotational j -level population distribution $w_j = \sum_{m=-j}^j \rho_{jm, jm}$ close to the entrance interface. The driving pulse amplitude is $E_0 = 10^8$ V/m and is plotted on the $j=0$ plane in arbitrary units.

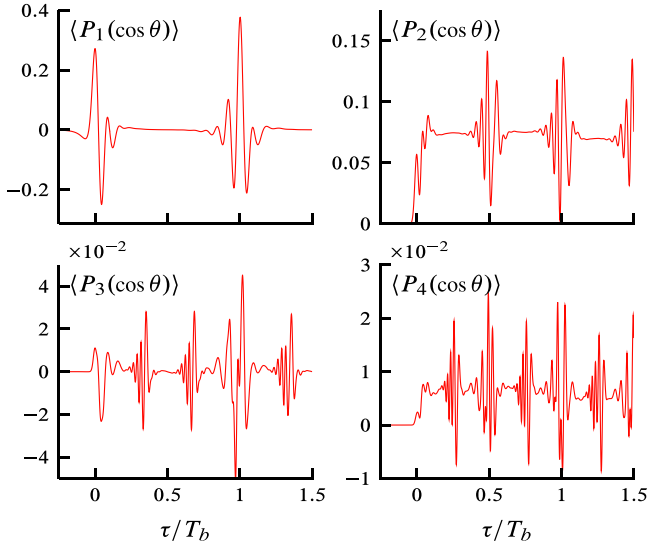


FIG. 9. (Color online) $\Theta_j^n \sim 1$: computer solution showing the first few Legendre moments $\langle P_k(\cos \theta) \rangle$ close to the entrance interface.

close to the entrance interface for the interval $\tau \in [-T_b/5, T_b/5]$. The time window contains the entire input pulse, which is shown with an arbitrary scale on the $j = 0$ plane. On the $\tau = -T_b/4$ plane, the height of the bars shows the initial Maxwell-Boltzmann distribution prior to the pulse interaction. We find that as the pulse enters into the medium, a significant amount of population is moved to higher rotational states, evidenced by a shift in the peak of w_j from $j = 5$ at $\tau = -T_b/5$ to $j = 10$ at $\tau = T_b/5$ in Fig. 8.

To examine the excitation of the molecules in greater detail and estimate the order of the excited rotational wave packet, Fig. 9 shows the evolution of the first few Legendre moments $\langle P_k(\cos \theta) \rangle$ over the first quantum beat period. Note that $\langle P_k(\cos \theta) \rangle$ are experimental observables, measurable by, e.g., photoelectron imaging [61], and offers good quantitative descriptions of the excited wavepacket. The maximum value of the first two moments in Fig. 9 are respectively $\langle P_1(\cos \theta) \rangle \approx 0.4$ and $\langle P_2(\cos \theta) \rangle \approx 0.15$, showing that the molecules are both orientated and aligned during the pulse interaction. The peak values of the higher moments are more modest, equal to $|\langle P_3(\cos \theta) \rangle| \lesssim 0.05$ and $|\langle P_4(\cos \theta) \rangle| \lesssim 0.025$, respectively. Moments of higher order are even smaller, with $\langle P_5(\cos \theta) \rangle_{\max} \sim 0.01$ and $\langle P_6(\cos \theta) \rangle_{\max} \sim 0.006$. Recalling that the Legendre moments of order κ contain coherences up to order $|j' - j| \leq \kappa$, we find that the excitation of the molecules at $x \gtrsim 0$ occurs as a multiphoton process up to approximately fourth order. Note that the molecules are not orientated at half-integer beat periods since $\langle P_1(\cos \theta) \rangle \approx 0$ for $\tau = (k + 1/2)T_b$.

To demonstrate the evolution of the molecular state in greater detail during the interaction with the pulse at the entrance interface, the panels in Fig. 10 show the probability density ϱ for various times τ/T_b . The temporal evolution of ϱ is observed by reading the panels from left to right, top to bottom. The panel $\tau/T_b = -0.05$ shows that the weak leading edge of the pulse pushes ϱ slightly down into the southern hemisphere, manifested by the appearance of a small

shift in the center of mass of ϱ towards the south pole. The panel immediately to the right shows the probability density at $\tau = 0$ and demonstrates that the rotor molecules are oriented with preferred direction $\theta < \pi/2$ due to the first carrier lobe. The sudden change in orientation from slightly towards $-z$ to strongly along $+z$ is due to the double leading lobe structure on the input pulse. The first, weakly negative carrier lobe will tend to weakly orient the molecules along $\theta = \pi$, while the first main carrier lobe, which is much stronger, acts to orient the rotor molecules along $\theta = 0$. When the field phase reverses at $\tau = 0$ and the subsequent large negative carrier lobe enters into the medium, the orientation is reversed and at $\tau/T_b = 0.05T_b$ the molecular axes point primarily into the southern hemisphere. The subsequent panels show the near field-free dephasing and rephasing of the molecules. From $\tau/T_b = 0.05$ to 0.5 , the rotor molecules gradually move away from being oriented to being aligned. At the quarter revival period $\tau/T_b = 0.25$, the orientation $\langle \cos \theta \rangle$ is approximately zero. At $\tau/T_b = 0.5$ then $\langle \cos \theta \rangle \approx 0$ but $\langle \cos^2 \theta \rangle \sim 0.1$ (see Fig. 9), showing that at half-integer quantum revival periods the molecules are aligned, but not orientated. The up-down symmetry of the molecules is therefore preserved at half-revival times, but not at integer revival times. Moving on from $\tau/T_b = 0.50$ and towards $\tau/T_b = 1$ the molecules gradually reorient in the absence of the pulse. We observe this for $\tau/T_b = 0.95$ where $\rho(\tau, x \approx 0; \theta)$ peaks at $\theta = \pi$, indicating that the majority of the rotor molecules are oriented along $-z$. A short time later, at $\tau/T_b = 1$, the ensemble is oriented along $+z$ as expected. The panel with $\tau = T_b$ in Fig. 10 may be contrasted with Fig. 6(b), which showed a corresponding plot in the linear interaction regime. Note that the orientation at $\tau/T_b = -0.05$ is weak compared to the orientation at $\tau/T_b = 0.95$, while the orientations at $\tau/T_b = 0$ and 1 are quantitatively comparable. The reason is that the temporal evolution up to $\tau/T_b = -0.05$ occurs in the linear regime, while the large degree of orientation along $-z$ at $\tau/T_b = 0.95$ is due to nonlinear interactions with the entire pulse.

Next, the spatiotemporal evolution of the THz field and the alignment $\langle \cos^2 \theta \rangle$ (measured as $\langle P_2 \cos \theta \rangle$) are presented in Fig. 11. Overall, we find that the pulse interacts nonlinearly only over the first few millimeters of the sample, and then falls back into the linear propagation regime. While not shown explicitly, we observe comparatively strong molecular orientations in this spatial region of the material where $\langle \cos \theta \rangle_{\max} \approx 0.3$, whereas $\langle \cos \theta \rangle_{\max} \sim 10^{-2}$ was found in the linear regime. Figure 11(b) shows the corresponding evolution for the molecular alignment. We recall that $\langle P_2(\cos \theta) \rangle = 0$ for molecules with isotropically distributed Zeeman levels and that $\langle P_2(\cos \theta) \rangle$ contains the Raman coherences $\rho_{jm, j\pm 2m}$ and population terms. We have also found that the population distribution is asymmetric in the Zeeman levels since $\langle \cos^2 \theta \rangle_{p, \max} \sim 0.38$, whereas a value of $1/3$ would be obtained for an isotropic population distribution. Such a result is expected because the transition dipole moments of the $m = 0$ ladder are larger than the $m \neq 0$ ladders, resulting in uneven excitations for different m levels. The rapid oscillations seen at half and integer revival times are due to the excitation of rotational Raman coherences, indicating the presence of two-photon resonant transitions of the type $j \rightarrow j + 1 \rightarrow j + 2$, as indicated earlier. From the data in Fig. 11(b) we note,

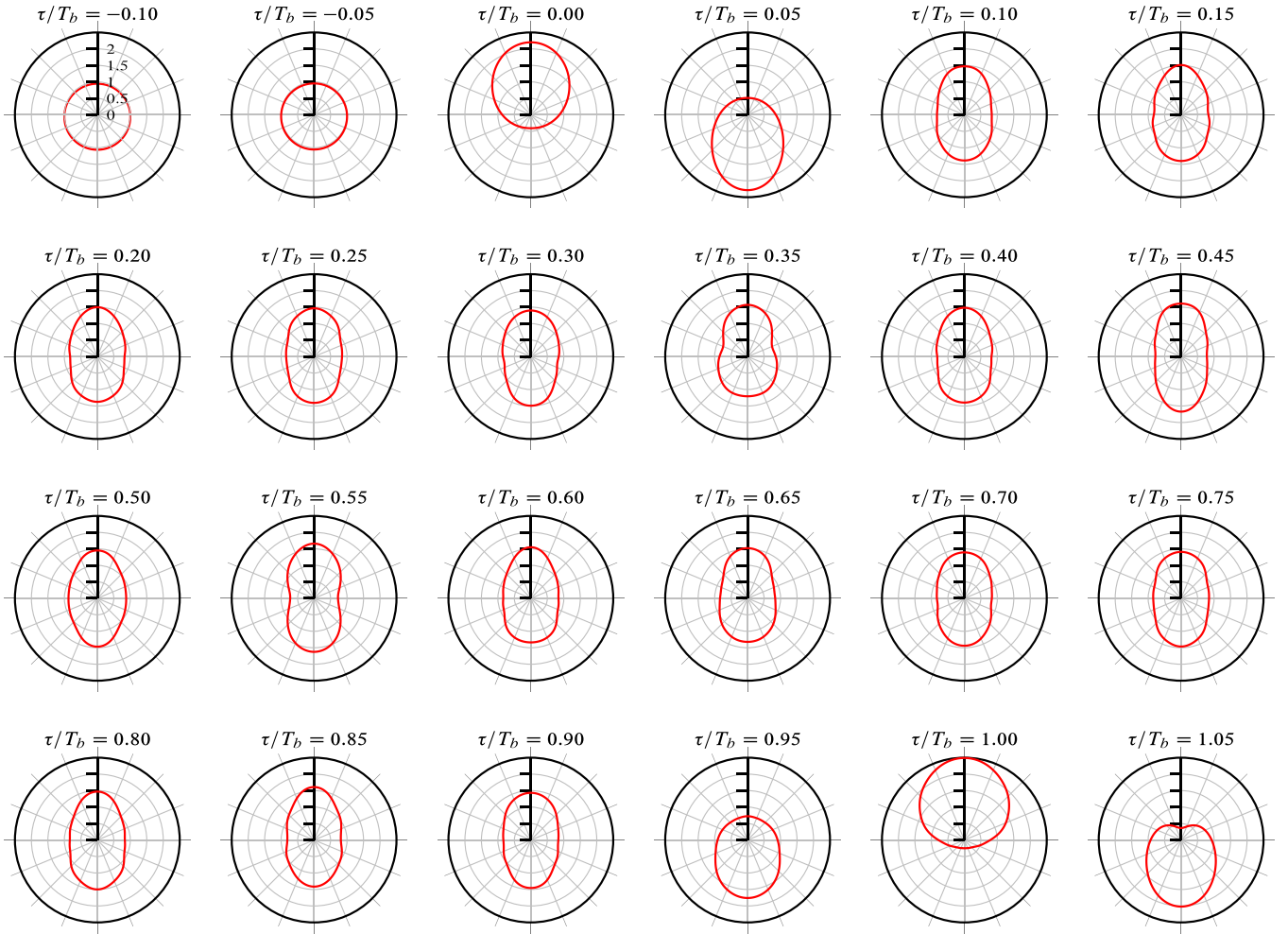


FIG. 10. (Color online) $\Theta_j^m \sim 1$: snapshots of the probability density at the entrance interface for various times τ for nonlinear excitation with a single-cycle THz pulse. The concentric circles indicate the value of ρ in units of $1/(4\pi)$ (see the top left panel).

importantly, that $\langle P_2(\cos\theta) \rangle \sim 0$ for $x > 1$ cm, showing that the pulse falls back into the linear interaction regime after only a short propagation distance.

B. Intermediate nonlinear regime $\Theta_j^m > 1$

Next, we consider the propagation of a pulse with amplitude $E_0 = 10^9$ V/m, which yields $\Theta_5^0 \approx 60$. The temporal resolution for this simulation is $\Delta\tau \approx 0.1$ fs, about six times higher than the critical sampling period $\Delta\tau_{\text{crit}} = \pi/\omega_j \approx 0.6$ fs required by the Nyquist-Shannon sampling theorem.

The excitation of the molecular interface with a single-cycle pulse of this magnitude results in an complex excitation of the medium. The data in Fig. 12(a) show the rotational state distribution w_j at the entrance interface during the interaction with the driving pulse. We observe that as the driving pulse excites the medium, the leading carrier lobe drives the population up to roughly $j \sim 30$. At the tail of this carrier lobe (before the zero crossing), part of the population is coherently returned to lower rotational orbitals, shown by the reappearance of population in lower j levels before $\tau = 0$. This effect will be discussed in greater detail below, but let us briefly mention that the process is due to coherent saturation

of the various rigid-rotor orbitals accessible by the pulse. In essence, the driving pulse is not sufficiently strong to drive population further up the rotational ladder and, as a result, energy is nonlinearly transferred from the medium and back to the pulse. Note that as the medium is essentially “pre-excited” by the time the second carrier lobe enters into the medium, population is transferred even higher up the rotational ladder, up to roughly $j = 36$ as shown in Fig. 12(a). After the driving pulse has passed, the population is distributed over roughly 27 rotational j levels, with $j = 10$ being most populated. The panels (b) and (c) in the same figure show the corresponding probability density for two time windows, one large enough to contain the first few quantum beat periods [(c)], and one that shows the temporal evolution around the driving pulse in greater detail (b). The solid line in each panel indicates the value of $\langle \cos\theta \rangle$, and is plotted versus the right vertical axis. Figure 12(b) shows that the maximum probability density at $\theta = 0$ near the leading edge of the input pulse at $\tau \lesssim 0$ is as high as 0.9, indicating that the molecules are strongly oriented along $+z$ by the leading positive lobe of the input pulse. At the same isochronic line ρ is approximately zero for $\theta \geq \pi/2$ and all the molecules are therefore found in the northern hemisphere. Note that the polarization is saturated

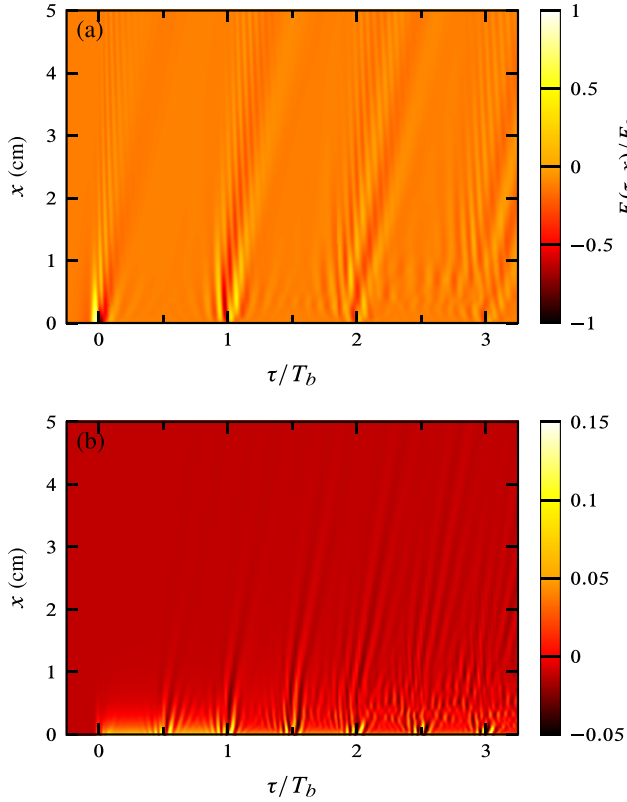


FIG. 11. (Color online) $\Theta_j^m \sim 1$: propagation with peak pulse amplitude $E_0 = 10^8$ V/m. (a) Spatiotemporal evolution of the electric field in units of E_0 . (b) Second Legendre moment $\langle P_2(\cos\theta) \rangle$.

whenever $\langle \cos\theta \rangle = 1$, whereas we observe $\langle \cos\theta \rangle_{\max} \approx 0.9$ in our computer simulations. When the trailing carrier lobe penetrates into the material, the orientation of the molecules is reverted so that they are pointing along $\theta = \pi$ with approximately zero probability of observing them along $\theta = 0$. After the pulse has passed, the subsequent dephasing of the rotor molecules shows that the probability density is higher at the poles $\theta = 0$ and π than at the equator $\theta = \pi/2$ showing that the molecules are aligned. Note that in the almost field-free dephasing of the molecules we also find that the molecules are weakly oriented since $\langle \cos\theta \rangle$ does not vanish at $\tau = T_b/2$ [see Fig. 12(c)]. Recalling that the expression for ρ contains all coherences ρ_{j_m, j'_m} , the rapid temporal oscillations and the accumulation of probability on the poles for $\tau \gtrsim 0$ shows that the molecules are excited into a coherent superposition of higher-order angular momentum states. The higher-order coherences oscillate rapidly in the absence of an external field and they are responsible for the complicated temporal structure of ρ observed in Figs. 12(b) and 12(c). The most likely explanation for the incomplete dephasing of the orientation $\langle \cos\theta \rangle$ observed in Fig. 12(c) at times between the pulse revivals times is that the molecules are excited into a wave packet with a dominant level (in this case $j = 10$), which prevents complete destructive interference in between wave packet revivals. We remark that by running computer simulations with even higher temporal and spatial resolutions (for much shorter propagation lengths and integration times), we have verified that the incomplete dephasing of $\langle \cos\theta \rangle$

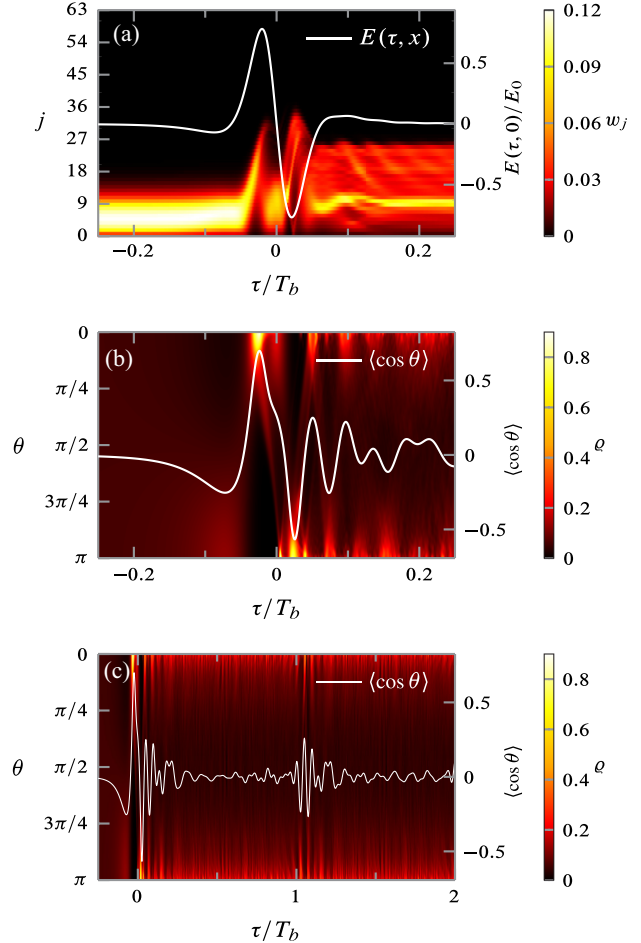


FIG. 12. (Color online) $\Theta_j^m > 1$: excitation with an input pulse with peak amplitude $E_0 = 10^9$ V/m. (a) Rotational state population w_j for $x \gtrsim 0$ during the action of the driving pulse. (b) and (c) Probability density ρ for $x \gtrsim 0$. (b) shows an inset of (c) for $\tau/T_b \in [-0.25, 0.25]$.

observed in Fig. 12(c) at half-integer quantum beat periods is not due to numerical errors.

Next, we examine the spatiotemporal evolution of the pulse and medium. Figures 13(a) and 13(b) show the field $E(\tau, z)$ and the orientation $\langle \cos\theta \rangle$ using the input pulse above. We find that the driving pulse propagates a substantially longer distance into the medium than in both the linear ($\Theta_{jm} \ll 1$) and weakly nonlinear ($\Theta_{jm} \sim 1$) regimes before it begins to disperse, approximately 4 cm before it falls back into the linear propagation regime. We also find that the orientation $\langle \cos\theta \rangle$ is maintained to a considerable degree; orientations as high as 0.9 are observed several centimeters into the medium. Note that although orientational revivals occur near the entrance interface [recall Fig. 12(c)], molecular rephasing is not observed further into the medium. We believe that the mechanism that leads to suppression of the orientational revivals further into the medium is the development of a comparatively long pulse tail over the first few millimeters of propagation in conjunction with saturation of the molecular orbitals. To show this, the reshaping of the electric field is presented in greater detail in the panels in Fig. 14. For comparison, the dashed line in

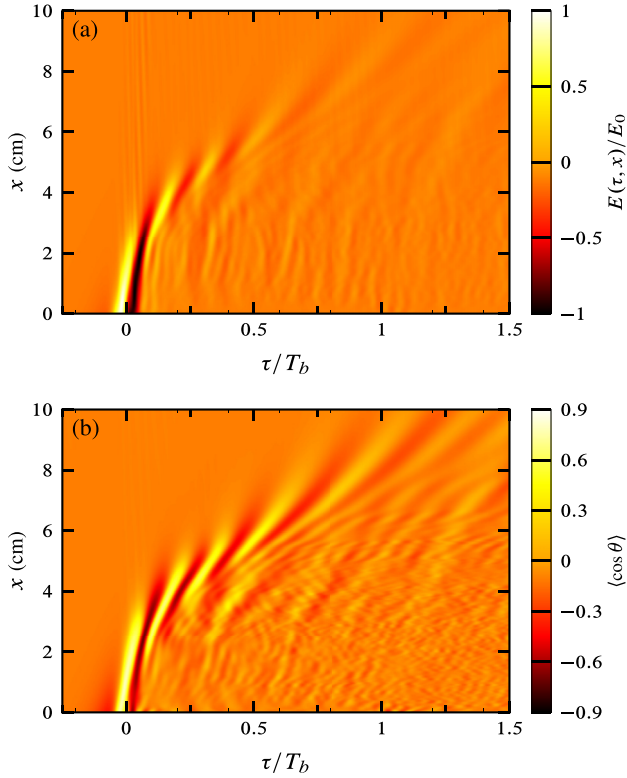


FIG. 13. (Color online) $\Theta_j^m > 1$: propagation of a single-cycle THz pulse with amplitude $E_0 = 10^9$ V/m. (a) The instantaneous electric field value $E(\tau, x)$ in units of E_0 . Dark and bright areas show regions with $E(\tau, x) < 0$ and $E(\tau, x) > 0$, respectively. (b) The orientation $\langle \cos \theta \rangle(\tau, x)$.

each panel shows the propagation of the same pulse in the linear interaction regime. We observe in Fig. 14(a) that a small pulse revival at $\tau = T_b$ has developed after a short propagation distance. Note that the relative amplitude of the revival is small in comparison with the predictions of the linear theory, which is understandably due to the fact that the orientation is close to saturation [$\langle \cos \theta \rangle \sim 0.9$ in Fig. 13(b)]. Thus the relative amplitude of the pulse revivals are expected to be weaker when the amplitude of the driving pulse is increased further. Moreover, the development of a transient tail on the driving pulse after a few millimeters of propagation leads to further deterioration of the pulse revivals. The rationale behind this is that further into the medium the molecules are no longer excited by a single “kick,” but interact with a pulse tail all the way up to $\tau = T_b$ and therefore do not dephase and rephase freely. As a result, molecular revivals occur only closest to the interface. Moreover, Figs. 13 and 14 show that the driving pulse is conserved to a considerable degree over the first few centimeters of propagation. We believe that the preservation is due to coherent saturation (i.e., bleaching), but the effect will be discussed in greater depth in the next section. Note that for both linear and nonlinear excitation, Fig. 14(e) predicts that only a high-frequency precursor remains of the driving pulse after propagating through the entire length of the medium. These fields are most likely composed of the nonresonant, high-frequency content of the input pulse spectrum.

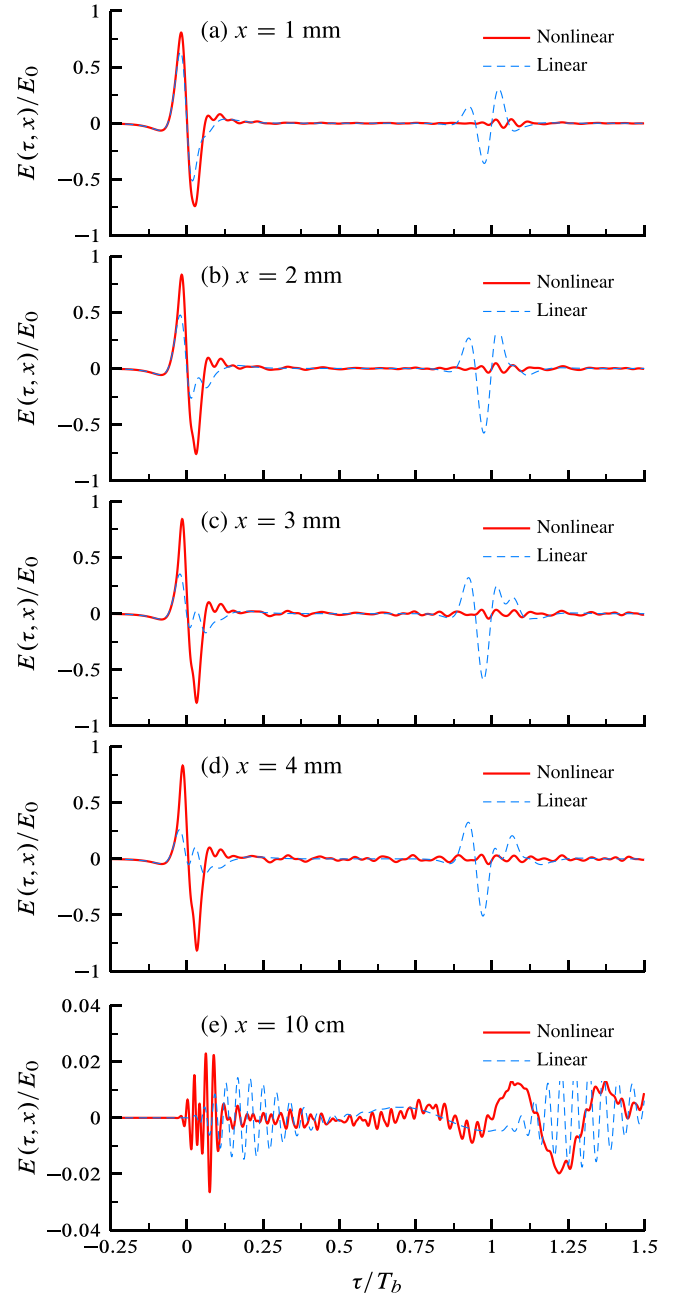


FIG. 14. (Color online) $\Theta_j^m > 1$: comparison of linear and nonlinear solutions. The solid and dashed lines show the temporal pulse profiles of initial pulses with amplitudes $E_0 = 10^9$ and 5×10^6 V/m, respectively.

C. Strongly nonlinear regime $\Theta_{jm} \gg 1$

Finally, we consider the propagation of a pulse with amplitude $E_0 = 5 \times 10^9$ V/m, which places this pulse in the strongly nonlinear regime $\Theta_5^0 \approx 1600$. Note that such pulses are presently only available from linear accelerators where field amplitudes as high as 4.4 GV/m have been reported [62].

Figure 15 shows the temporal evolution of the population distribution w_j on the interface $x \gtrsim 0$. We observe that as the pulse enters into the material, the molecules are excited to higher orbitals, up to $j \sim 72$. Furthermore, we observe also that under both the leading and trailing carrier lobes the

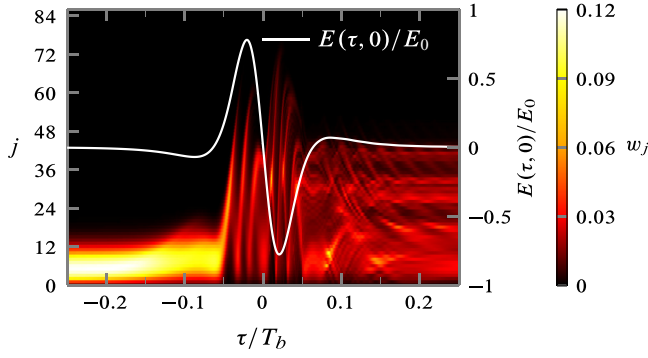


FIG. 15. (Color online) $\Theta_j^m \gg 1$: population distribution (color coded) for excitation with an initial single-cycle pulse with normalized area $\Theta_5^0 \approx 1600$. The solid line shows the pulse in units of E_0 .

molecules are also coherently returned to lower orbitals during interaction with the pulse. Note that coherent energy return was observed also in the linear interaction regime, but then due to a rapid sign reversal of the electric field. Here, the return process occurs under a single carrier lobe and is therefore of a distinctly different physical origin. To the best of our knowledge, these types of excitation and de-excitation patterns have not been observed earlier, and thus represent a new nonlinear optical effect. While a thorough discussion of this effect is outside the scope of this report, we believe that these types of oscillations are related to Rabi oscillations, which normally take place when a long pulse coherently saturates a single atomic line transition. These types of oscillations impress themselves quite remarkably on the propagated field. Here, recalling Eq. (20) for convenience,

$$\epsilon_0 c \frac{\partial^2 E^2(\tau, x)}{\partial x} = -\mathcal{N} \frac{\partial \langle H_0 \rangle}{\partial \tau}, \quad (83)$$

which shows that when $\langle H_0 \rangle$ decreases one expects corresponding amplification of E , and vice versa.

Figure 16 shows the spatiotemporal evolution of the electric field and the molecular orientation. We find that the pulse maintains its single-cycle structure to a considerable degree for propagation through the entire length of the medium. Some features deserve particular mention. Firstly, we observe that the two main carrier lobes are temporally compressed for increasing propagation distances. Secondly, we find that the pulse develops self-oscillations superimposed on top of the two carrier lobes, which is, for example, seen on the trailing carrier lobe around $x = 1$ cm in Fig. 16(a). Thirdly, we observe the formation of a comparatively strong and oscillating pulse tail which has no clear spatiotemporal structure. The pulse tail reaches amplitudes as high as $0.4E_0$ and therefore interacts strongly with the medium. Fourthly, we find that the leading edge (i.e., before the leading carrier lobe) is sufficiently strong to preorient the molecules prior to the arrival of the first carrier lobe, and this part of the pulse is therefore absorbed according to Eq. (20).

To examine the above mentioned features in greater details, Fig. 17 shows the temporal evolution of $E(\tau, x)$ and $\langle H_0 \rangle$ sampled at various positions in the medium. We find that as the pulse enters into the medium, the internal energy $\langle H_0 \rangle$ of the medium is saturated, evidenced by the appearance of several

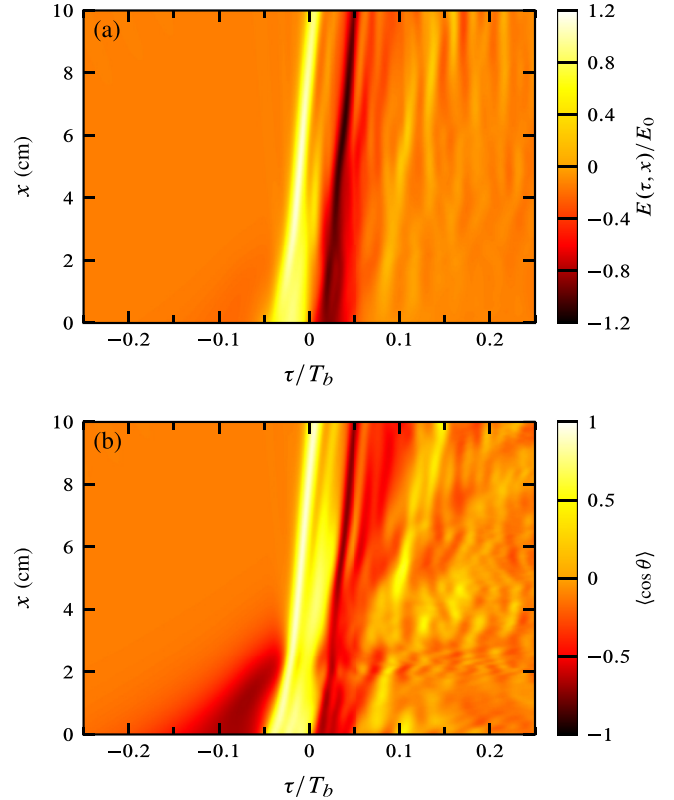


FIG. 16. (Color online) $\Theta_j^m \gg 1$: spatiotemporal evolution of $E(\tau, x)$ and $\langle \cos \theta \rangle$.

temporal peaks in $\langle H_0 \rangle$ [see, e.g., Fig. 17(a)]. The leading bump in $\langle H_0 \rangle$ observed in Fig. 17(a) around $\tau \sim -0.1T_b$ is due to coherent energy return occurring when E switches from negative to positive on the leading edge of the pulse, consistent with the linear analysis. The larger, more rapid, oscillations seen under the first carrier lobe are due to the nonlinear effect mentioned above. As the pulse propagates deeper into the material, its leading edge is always absorbed since the molecules are prepared as absorbers. However, if the leading edge is sufficiently strong to saturate the molecular orbitals that are accessible by the pulse, the next slice of pulse that enters into this region will be amplified rather than absorbed, a process that leads to self-steepening of the pulse. Then, if this “next slice of pulse” is sufficiently strong to repeatedly saturate the medium, this process may repeat itself several times under each carrier lobe such that a number of self-oscillations impress themselves on top of each of the two carrier lobes [see, e.g., Fig. 17(b)]. Further propagation tends to enhance this reshaping process: as the pulse propagates deeper into the medium, its spectrum broadens due to self-steepening, opening up the possibility of excitations into even higher orbitals. Saturation of higher orbitals leads to an increase in the peak values of $\langle H_0 \rangle$ that are reached during interaction with the pulse. This reinforces the propagation-induced self-steepening process and leads to a weak optical shock near the leading pulse edge. This feature is particularly prominent in Figs. 17(c) and 17(d), where the leading edge is both steepened and amplified. We remark that the shock formation process can not proceed indefinitely because residual energy is always present in the excited molecules after the pulse has passed. Thus the spectral

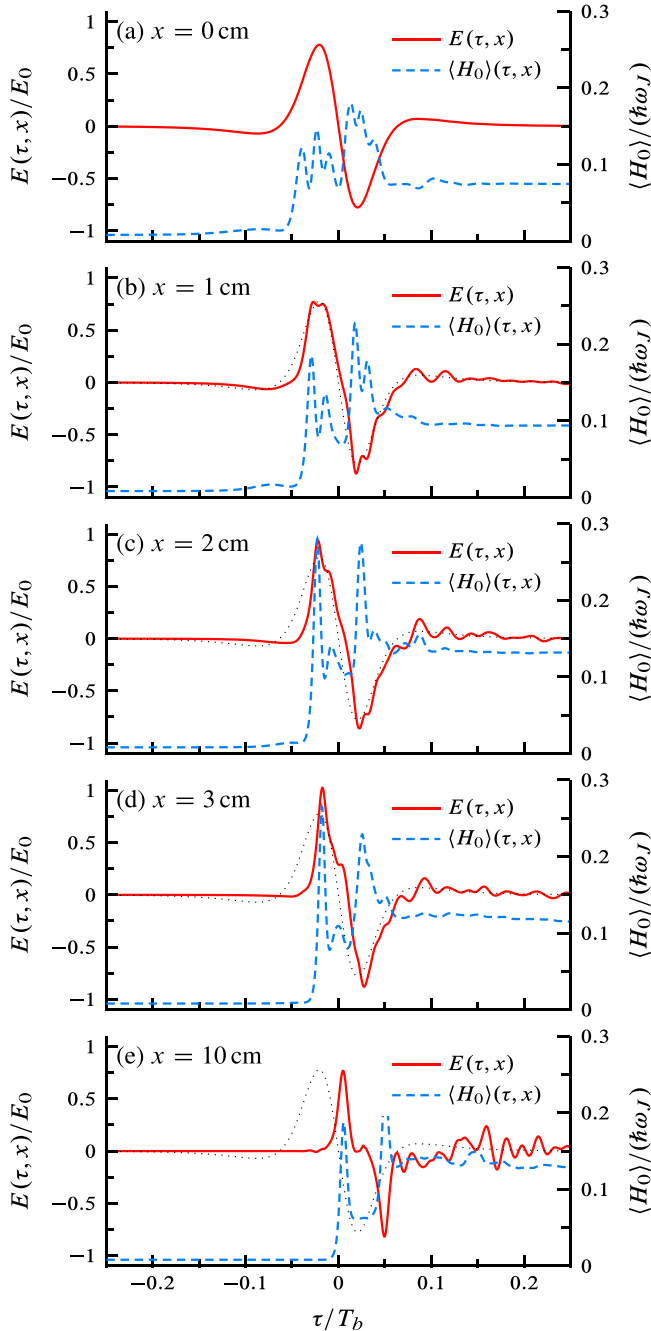


FIG. 17. (Color online) $\Theta_j^m \gg 1$: propagation with $E_0 = 5 \times 10^9$ V/m. The panels show the electric field profiles (solid line, plotted against the left vertical axis) and the internal molecular energy $\langle H_0 \rangle$ (dashed line, plotted against the right vertical axis) in units of $\hbar\omega_J$ for various propagation lengths x . For comparison, the dotted line in (b)–(e) shows the input pulse.

broadening of the pulse comes at the cost of lost energy. Qualitatively speaking, one eventually reaches a break-even point where the reshaped pulse $E(\tau, x)$ does not contain a sufficient amount of energy to lead to further developments of a leading edge shock. In Fig. 17, which shows the internal energy $\langle H_0 \rangle$ at the exit interface $x = 10$ cm, the achieved peak values of $\langle H_0 \rangle$ are smaller than at $x = 3$ cm, for example. However, from experience gained through computer simulations, we

anticipate that even more pronounced optical carrier shocks will form when considering input pulses with even higher amplitude.

Transparency of the driving pulse is not observed here since the final energy state is $\langle H_0 \rangle(\tau, x) > \langle H_0 \rangle(\tau \rightarrow -\infty, x)$ for all positions x . However, observe that the driving pulse energy is conserved to a considerable extent when compared to the linear regime where dispersion led to temporal broadening of the driving pulse as well as the pulse revivals. The energy of the field shown in the bottom panel in Fig. 17 represents approximately 80% of the input pulse energy. Here, the “energy” of the driving pulse is defined as the fluence delivered in the time window $[-T_b/2, T_b/2]$. This is in stark contrast to the linear regime where less than 2% of the energy of the driving pulse was preserved in the same time window after exiting the medium. As might be expected, the preservation of the fluence is due to saturation effects. Scaling Eq. (20) by E_0^2 leads to

$$\frac{\partial}{\partial x} \mathcal{E}^2(\tau, x) = -\frac{1}{\epsilon_0 c E_0^2} \frac{\partial U}{\partial \tau}, \quad (84)$$

where $\mathcal{E} = E/E_0$ is a quantity of order unity. In the linear regime $U \propto E_0^2$ [see Eq. (37)], hence, the effective absorption length scale is constant in the linear regime. When U is saturated, further increasing E will result in coherent energy return rather than increased absorption. The pulse behavior in Fig. 17 is therefore the result of *coherent bleaching* of the medium.

VI. CONCLUSIONS

In summary, we introduce and analyze a unidirectional many-level Maxwell-Bloch model describing the evolution of single-cycle THz pulses propagating through a spatially extended collection of quantum-mechanical rigid-rotor molecules. Analytical time-domain solutions are derived in the linear propagation regime, showing that the pulse evolves into a series of dispersive pulse revivals that broaden temporally with increased propagation distance. Analogous dispersion occurs for the molecular orientation. In the special case of equal line strengths, the evolution has only one length scale and the pulse evolves into a pulse train, where each impulse is an exact temporal copy of the input pulse decaying algebraically with propagation distance. Furthermore, the linearized solutions are shown to represent the superposition of linear 0π pulses in the sharp-line limit.

We report on an efficient, scalable numerical algorithm for spatiotemporal integration of the reduced Maxwell-Bloch equations. The method is applicable to propagation of single-cycle pulses in many-level media over long distances. With the exception of subspace decomposition, which is used to reduce the numerical cost for rigid-rotor molecules, the algorithm [Eqs. (68) and (72)] is immediately extendable to other types of atomic or molecular Bloch systems. Thus a significant result of this paper is the extension of existing pulse propagation algorithms to the single-cycle many-level regime.

Computer solutions for a few case studies of nonlinear propagation are presented. In the nonlinear regime, we find that the rotor molecules are strongly oriented by the input pulse and orientations as high as 0.9 are observed. Compared with the linear propagation regime, the spatiotemporal evolution in the

nonlinear regime shows that the driving pulse is preserved to a considerable extent during propagation and penetrates deep into the medium. Correspondingly, the pulse revivals are of considerably lower relative amplitude in the nonlinear versus the linear regime. In the far-field, high-frequency precursor fields are observed when the medium is initially in thermal equilibrium. For sufficiently strong pulses, coherent bleaching of the medium leads to self-steepening and carrier-shock formation, as well as improved transmission of the driving pulse. Although our motivation for undertaking this study derives from an interest in the underlying physics, the results are also of practical interest. For example, our results relate closely to investigations of molecular orientation of spatially extended media. The ability of nonlinear THz pulses to penetrate further into materials is also of some relevance in transmission and reflection imaging of tissue.

We also mention that some of the results presented in this paper that addresses the molecular state at $x = 0$ have been predicted by others. For example, the data in Fig. 4 have been predicted by Fleischer *et al.* [7], and some of the data in Fig. 10 have been predicted by Henriksen [5]. While our data offer a generally favorable comparison with earlier publications, few results pertaining to propagation of THz pulses in spatially extended, resonant media have been published to date. The numerical calculations presented here predict the existence of new nonlinear optical effects,

but the numerical results are by no means exhaustive. More thorough theoretical and experimental efforts are called for in order to fully understand the nonlinear dynamics of the types of systems that we consider here. Among these, the most immediate investigations should account for the influence of different ambient temperatures (affecting the initial distribution of the population), different pulse shapes (for example, through the carrier-envelope phase), and investigations of dual-pulse excitations. In addition, our model is open to theoretical extensions. These include the incorporation of centrifugal distortion and the inclusion of decoherence. Note that incorporation of decoherence couples the various ladder systems through the possibility of m -changing molecular collisions, allowing for population transfer between them. However, collision processes are incoherent and therefore do not affect the subspace decomposition.

ACKNOWLEDGMENTS

This work was partially supported by the Norwegian University of Science and Technology with computational resources provided by NOTUR, the Norwegian Metacenter for Computational Science. The authors thank the referee for insightful suggestions and for providing several pertinent references.

-
- [1] T. Kampfrath, K. Tanaka, and K. A. Nelson, *Nat. Photon.* **7**, 680 (2013).
 - [2] X. Yin, B. Ng, and D. Abbott, *Terahertz Imaging for Biomedical Applications: Pattern Recognition and Tomographic Reconstruction* (Springer-Verlag, New York, 2012).
 - [3] M. C. Beard, G. M. Turner, and C. A. Schmuttenmaer, *J. Phys. Chem. B* **106**, 7146 (2002).
 - [4] Y. Yang, M. Mandehgar, and D. Grischkowsky, *Opt. Express* **22**, 4388 (2014).
 - [5] N. E. Henriksen, *Chem. Phys. Lett.* **312**, 196 (1999).
 - [6] M. Machholm and N. E. Henriksen, *Phys. Rev. Lett.* **87**, 193001 (2001).
 - [7] S. Fleischer, Y. Zhou, R. W. Field, and K. A. Nelson, *Phys. Rev. Lett.* **107**, 163603 (2011).
 - [8] M. Lapert and D. Sugny, *Phys. Rev. A* **85**, 063418 (2012).
 - [9] J. Ortigoso, *J. Chem. Phys.* **137**, 044303 (2012).
 - [10] S. Fleischer, R. W. Field, and K. A. Nelson, *Phys. Rev. Lett.* **109**, 123603 (2012).
 - [11] C.-C. Shu and N. E. Henriksen, *Phys. Rev. A* **87**, 013408 (2013).
 - [12] Z.-Y. Zhao, Y.-C. Han, Y. Huang, and S.-L. Cong, *J. Chem. Phys.* **139**, 044305 (2013).
 - [13] K. Kitano, N. Ishii, N. Kanda, Y. Matsumoto, T. Kanai, M. Kuwata-Gonokami, and J. Itatani, *Phys. Rev. A* **88**, 061405 (2013).
 - [14] K. N. Egodapitiya, S. Li, and R. R. Jones, *Phys. Rev. Lett.* **112**, 103002 (2014).
 - [15] S.-L. Liao, T.-S. Ho, H. Rabitz, and S.-I. Chu, *Phys. Rev. A* **87**, 013429 (2013).
 - [16] C. Qin, Y. Liu, X. Zhang, and T. Gerber, *Phys. Rev. A* **90**, 053429 (2014).
 - [17] T. K. Cheng, L. H. Acioli, J. Vidal, H. J. Zeiger, G. Dresselhaus, M. S. Dresselhaus, and E. P. Ippen, *Appl. Phys. Lett.* **62**, 1901 (1993).
 - [18] T. Kampfrath, A. Sell, G. Klatt, A. Pashkin, S. Mahrlein, T. Dekorsy, M. Wolf, M. Fiebig, A. Leitenstorfer, and R. Huber, *Nat. Photon.* **5**, 31 (2011).
 - [19] K. F. Lee, D. M. Villeneuve, P. B. Corkum, and E. A. Shapiro, *Phys. Rev. Lett.* **93**, 233601 (2004).
 - [20] S. Fleischer, I. S. Averbukh, and Y. Prior, *J. Phys. B* **41**, 074018 (2008).
 - [21] C. Wu, G. Zeng, Y. Gao, N. Xu, L.-Y. Peng, H. Jiang, and Q. Gong, *J. Chem. Phys.* **130**, 231102 (2009).
 - [22] I. V. Litvinyuk, K. F. Lee, P. W. Dooley, D. M. Rayner, D. M. Villeneuve, and P. B. Corkum, *Phys. Rev. Lett.* **90**, 233003 (2003).
 - [23] R. Velotta, N. Hay, M. B. Mason, M. Castillejo, and J. P. Marangos, *Phys. Rev. Lett.* **87**, 183901 (2001).
 - [24] H. Harde, S. Keiding, and D. Grischkowsky, *Phys. Rev. Lett.* **66**, 1834 (1991).
 - [25] H. Harde and D. Grischkowsky, *J. Opt. Soc. Am. B* **8**, 1642 (1991).
 - [26] J. P. Palastro, T. M. Antonsen, and A. Pearson, *Phys. Rev. A* **84**, 013829 (2011).
 - [27] R. W. Ziolkowski, J. M. Arnold, and D. M. Gogny, *Phys. Rev. A* **52**, 3082 (1995).
 - [28] M. Wu, S. Chen, K. J. Schafer, and M. B. Gaarde, *Phys. Rev. A* **87**, 013828 (2013).

- [29] J. R. Freeman, J. Maysonnave, S. Khanna, E. H. Linfield, A. G. Davies, S. S. Dhillon, and J. Tignon, *Phys. Rev. A* **87**, 063817 (2013).
- [30] P. Kumar and A. K. Sarma, *Phys. Rev. A* **85**, 043417 (2012).
- [31] B. Bidégaray, A. Bourgeade, and D. Reignier, *J. Comp. Phys.* **170**, 603 (2001).
- [32] C. Besse, B. Bidégaray-Fesquet, A. Bourgeade, P. Degond, and O. Saut, *ESAIM: Math. Modell. Num. Anal.* **38**, 321 (2004).
- [33] F. Schlottau, M. Piket-May, and K. Wagner, *Opt. Express* **13**, 182 (2005).
- [34] R. Marskar and U. Österberg, *Opt. Express* **19**, 16784 (2011).
- [35] T. Brabec and F. Krausz, *Phys. Rev. Lett.* **78**, 3282 (1997).
- [36] M. Geissler, G. Tempea, A. Scrinzi, M. Schnürer, F. Krausz, and T. Brabec, *Phys. Rev. Lett.* **83**, 2930 (1999).
- [37] M. Kolesik, J. V. Moloney, and M. Mlejnek, *Phys. Rev. Lett.* **89**, 283902 (2002).
- [38] P. Kinsler, S. B. P. Radnor, and G. H. C. New, *Phys. Rev. A* **72**, 063807 (2005).
- [39] P. Kinsler, *Phys. Rev. A* **81**, 013819 (2010).
- [40] L. Roso-Franco, *Phys. Rev. Lett.* **55**, 2149 (1985).
- [41] W. Forysiak, R. G. Flesch, J. V. Moloney, and E. M. Wright, *Phys. Rev. Lett.* **76**, 3695 (1996).
- [42] R. Marskar and U. L. Österberg, *Phys. Rev. A* **89**, 023828 (2014).
- [43] R. K. Bullough, P. M. Jack, P. W. Kitchenside, and R. Saunders, *Phys. Scr.* **20**, 364 (1979).
- [44] A. E. Kaplan, *J. Opt. Soc. Am. B* **15**, 951 (1998).
- [45] J. C. Eilbeck, J. D. Gibbon, P. J. Caudrey, and R. K. Bullough, *J. Phys. A* **6**, 1337 (1973).
- [46] R. K. Bullough, P. J. Caudrey, J. C. Eilbeck, and J. D. Gibbon, *Opt. Quantum Electron.* **6**, 121 (1974).
- [47] P. Bernath, *Spectra of Atoms and Molecules* (Oxford University Press, Oxford, 2005).
- [48] R. W. Boyd, in *Nonlinear Optics*, edited by R. W. Boyd (Academic Press, San Diego, CA, 1992).
- [49] S. Ramakrishna and T. Seideman, *Phys. Rev. Lett.* **95**, 113001 (2005).
- [50] M. D. Crisp, *Phys. Rev. A* **1**, 1604 (1970).
- [51] M. Abramowitz and I. Stegun, *Handbook of Mathematical Functions* (Dover Publications, New York, 1965).
- [52] J. Arlt, C. Weiss, G. Torosyan, and R. Beigang, *Phys. Rev. Lett.* **79**, 4774 (1997).
- [53] M. Kolesik and J. V. Moloney, *Rep. Prog. Phys.* **77**, 016401 (2014).
- [54] A. Tarasishin, S. Magnitskii, V. Shuvaev, and A. Zheltikov, *Opt. Express* **8**, 452 (2001).
- [55] H. Leblond and D. Mihalache, *Phys. Rep.* **523**, 61 (2013).
- [56] For initial states $\rho^{(m)} = \rho^{(-m)}$, it is only necessary to solve for $m \geq 0$ since $\mathcal{H}^{(m)} = \mathcal{H}^{(-m)}$. We choose to solve for $m = -J, -J + 1, \dots, J$ to avoid loss of generality.
- [57] D. Sugny, S. Vranckx, M. Ndong, N. Vaeck, O. Atabek, and M. Desouter-Lecomte, *Phys. Rev. A* **90**, 053404 (2014).
- [58] A. April, in *Ultrashort, Strongly Focused Laser Pulses in Free Space* (InTech, Rijeka, Croatia, 2010), Chap. 16, pp. 356–382.
- [59] E. Varoquaux, G. A. Williams, and O. Avenel, *Phys. Rev. B* **34**, 7617 (1986).
- [60] J. E. Rothenberg, D. Grischkowsky, and A. C. Balant, *Phys. Rev. Lett.* **53**, 552 (1984).
- [61] Y.-i. Suzuki and T. Seideman, *J. Chem. Phys.* **122**, 234302 (2005).
- [62] Z. Wu, A. S. Fisher, J. Goodfellow, M. Fuchs, D. Daranciang, M. Hogan, H. Loos, and A. Lindenberg, *Rev. Sci. Instrum.* **84**, 022701 (2013).